HHS Public Access

Author manuscript

Nature. Author manuscript; available in PMC 2024 April 03.

Published in final edited form as:

Nature. 2023 July ; 619(7968): 151–159. doi:10.1038/s41586-023-06217-y.

PD-1 maintains CD8 T cell tolerance towards cutaneous neoantigens

Martina Damo[1], **Noah I. Hornick**[1,2], **Aarthi Venkat**[3], **Ivana William**[1], **Kathryn Clulo**[1], **Srividhya Venkatesan**[1], **Jiaming He**[1], **Eric Fagerberg**[1], **Jennifer L. Loza**[1], **Darwin Kwok**[1], **Aya Tal**[1], **Jessica Buck**[1], **Can Cui**[1], **Jaiveer Singh**[1], **William E. Damsky**[2,4], **Jonathan S. Leventhal**[2], **Smita Krishnaswamy**[3], **Nikhil S. Joshi**[1,*]

[1]Department of Immunobiology, Yale University School of Medicine, New Haven, CT, 06519, USA

[2]Department of Dermatology, Yale University School of Medicine, New Haven, CT, 06519, USA

[3]Departments of Genetics and of Computer Science, Yale University School of Medicine, New Haven, CT 06519, USA

[4]Department of Pathology, Yale University School of Medicine, New Haven, CT, 06519, USA

Summary

The peripheral T cell repertoire of healthy individuals contains self-reactive T cells[1,2]. Checkpoint receptors like PD-1 are thought to allow the induction of peripheral tolerance by deletion or anergy of self-reactive CD8 T cells[7–14], however this model is challenged by the high frequency of immune-related Adverse Events (irAEs) in checkpoint receptor inhibitor-treated cancer patients[15].

We developed a novel mouse model where skin-specific expression of T cell antigens (Ags) in the epidermis caused local infiltration of Ag-specific CD8 T cells with an effector gene expression profile. In this setting, PD-1 allowed maintenance of skin tolerance by preventing tissue-infiltrating Ag-specific effector CD8 T cells from 1) acquiring a fully functional, pathogenic differentiation state, 2) secreting significant amounts of effector molecules, and 3) gaining access to epidermal Ag-expressing cells. In the absence of PD-1, epidermal Ag-expressing cells were eliminated by Ag-specific CD8 T cells resulting in local pathology.

*Corresponding author: Correspondence and requests for materials should be addressed to Nikhil S. Joshi. nikhil.joshi@yale.edu.

Declaration of competing interests

The authors declare no competing interests.

Additional information

Source data are provided with this paper.

Supplementary Information is available for this paper.

Code availability

The custom code used in this article for quantification of epidermal thickness can be accessed at https://github.com/dakwok/The-Histological-Inflammation-Computation-software.

The custom code used in this article for analysis of scRNAseq data with PHATE (scprep package) can be accessed at https://github.com/krishnaswamylab/scprep.

The custom code used in this article for analysis of scRNAseq with MAGIC can be accessed at https://github.com/KrishnaswamyLab/magic.

The CellPhoneDB algorithm can be accessed at cellphonedb.org.

The custom code used in this article for analysis of scRNAseq data with the MELD package can accessed at https://github.com/KrishnaswamyLab/MELD.

Transcriptomic analysis of skin biopsies from two patients with cutaneous lichenoid irAEs showed presence of clonally expanded effector CD8 T cells in both lesional and non-lesional skin. Thus, our data support a model of peripheral T cell tolerance where PD-1 allows Ag-specific effector CD8 T cells to co-exist with Ag-expressing cells in tissues without immunopathology.

Introduction

Extra-thymic peripheral T-cell tolerance prevents aberrant responses by CD8 T cells specific for self-antigens (Ags) or harmless non-self-Ags[1,2]. Both T-cell intrinsic (anergy and clonal deletion) and extrinsic (regulatory T cell (Treg)-mediated) mechanisms contribute to peripheral tolerance[3]. Anergy and clonal deletion directly shape the peripheral T cell repertoire by restraining and eliminating potentially pathogenic T cells, respectively[4]. Molecular signatures of anergy and clonal deletion are characterized by *failure* to acquire effector functions or infiltrate Ag-expressing tissues, and result from tolerogenic Ag presentation by dendritic cells (DCs) in peripheral lymphoid organs[5,6]. Peripheral tolerance breaks down in the absence of inhibition by checkpoint receptors (e.g., PD-1 and CTLA-4), resulting in the presence of effector CD8 T cells[7–12]. However, while checkpoint receptor blockade during peripheral tolerance *induction* generates effector CD8 T cells, CD8 T cell anergy is not rescued by checkpoint receptor blockade once established[13,14]. This suggests a binary process for peripheral tolerance induction in which checkpoint receptors determine whether tolerogenic DCs drive differentiation of the CD8 T cells towards either a tolerant *or* an effector state.

Immunotherapy with checkpoint receptor inhibitors (CPIs) results in immune-related Adverse Events (irAEs) in up to 70% of cancer patients[15]. irAEs are tisue-specific autoimmune-like side effects that often correlate with increased T cell infiltration into affected tissues and, in some cases, increases in T cell clonality[16–20]. Notably, irAEs affect such a large fraction of patients that it is unlikely that all irAEs are due to CPI-mediated exacerbation of ongoing (sub-clinical) autoimmune processes[21]. This suggests that CPIs could drive the breakdown in peripheral tolerance by inducing pathogenic Ag-specific T cell responses in non-autoimmune prone settings. Yet, this occurs at a time in life when anergy and deletion *should* have pruned the peripheral T cell repertoire of pathogenic self-reactive T cells. This raises questions about whether immunologically healthy subjects have self-reactive T cells that are kept functionally tolerant *because* of checkpoint receptor-mediated inhibition.

Limitations in experimental models, including leaky Ag-expression in thymus that results in deletion of Ag-specific endogenous CD8 T cells and increased Treg generation, have made it difficult to dissociate peripheral and central tolerance mechanisms, and thus, have hindered our understanding of physiological peripheral tolerance mechanisms[5–14,22]. To overcome these limitations, we developed the iNversion INducible Joined neoAntigen (NINJA) mouse, which allows for *de novo* induction of Ag expression in any peripheral tissue, without the confounding influence of thymic tolerance on endogenous CD4 or CD8 T cells[23]. NINJA mice are on a non-autoimmune prone C57BL/6 (B6) background, and thus we expect that Ag induction in NINJA mice will result in peripheral tolerance via anergy or deletion

of Ag-specific CD8 T cells. We previously observed that endogenous Ag-specific CD8 T cells accumulated in skin following local NINJA Ag expression without development of cutaneous pathology[23]. Here, we use this model to study mechanisms of tolerance towards skin-expressed Ags, investigate how cutaneous pathogenic responses are prevented and explore the involvement of checkpoint receptors in these processes.

Results

Checkpoint function in skin tolerance

To study the immunological outcome of *de novo* expression of peripheral Ags in the skin, we bred "N/C" (*Rosa26-NINJA/CreER*^{T2};*CAG-rtTA3 Tg*) mice [23,24]. In N/C mice, treatment with doxycycline (Dox)-containing food and topical 4-hydroxy-tamoxifen (4-OH-Tam; applied on a selected area of the skin indicated by the red box in Fig 1A) induced genetic recombinations that resulted in the expression of LCMV-derived $GP_{33–43}$ (GP33) and $GP_{61–80}$ (GP61) contained within GFP (Fig 1A and Extended Data Fig 1A). Flow cytometric analysis 15 days after initiating Dox/4-OH-Tam treatment showed that 15 ± 4% of skin cells from N/C were GFP+ (Ag-expressing), with 85 ± 2% of these being EpCAM+CD45- keratinocytes (Fig 1B and Extended Data Fig 1B). Confocal microscopy confirmed that GFP expression in the N/C model was limited to the epidermal layer of the skin (Fig 1C).

To test if checkpoint receptors regulated immunological tolerance in this model, N/C mice receiving Dox/4-OH-Tam (henceforth referred to as "Ag ON" mice, as opposed to "Ag OFF" negative control mice: either B6 mice, Dox/4-OH-Tam-treated NINJA mice, or untreated N/C mice) were also treated with anti-PD-1 and anti-CTLA-4 blocking antibodies ("Ag ON/CPI", Fig 1A). Ag ON/CPI mice presented overt cutaneous pathology localized to the Ag-expressing skin area (Fig 1D). To quantify disease severity in our model, we developed a pathological scoring system from 0–300, evaluating local appearance of erythema, lichenification and erosion/ulceration[25]. Mice with normal skin had a pathological score of 0, while scores from 1–15, 16–50, and >50 indicated mild, moderate, and severe cutaneous disease, respectively (Extended Data Fig 1C). Pathological scores in negative control mice ranged from 0–10 (median = 0), while in Ag ON mice scores ranged from 0–40 (median = 2.5; Fig 1E and Extended Data Fig 1D). Notably, Ag-expressing skin in 83% of Ag ON mice appeared normal or had signs of mild pathology, while Ag-expressing skin in 17% of Ag ON mice had moderate skin pathology (Extended Data Fig 1D). By contrast, the pathological scores in Ag ON/CPI mice were significantly higher, ranging from 10–130 (median = 90) (Fig 1E). Here, 28% of Ag ON/CPI had mild cutaneous disease, while the remaining 72% had moderate or severe cutaneous disease (Extended Data Fig 1D).

Histologically, cutaneous pathology in Ag ON/CPI mice was characterized by thickening of the epidermis and stiffening of the dermis (Fig 1F). Epidermal thickness quantification confirmed significant increases in Ag ON/CPI mice (24 ± 7μm) vs. Ag ON mice (14 ± 2μm) or negative controls (14 ± 2μm) (Fig 1G) and Keratin-10 staining showed visible disruption of epidermal structure in Ag ON/CPI samples (Fig 1H). Thus, *de novo* skin-specific expression of T cell Ags and CPI treatment led to localized cutaneous disease in the N/C model.

CPIs cause elimination of Ag+ skin cells

Ag-expression in skin was associated with local infiltration of T cells in both Ag ON and Ag ON/CPI mice (Fig 2A). Unlike CD4 T cells, CD8 T cells infiltrating the Ag-expressing skin in Ag ON and Ag ON/CPI mice were significantly increased compared to negative controls (25.8 ± 19.2 and 61.4 ± 47.1 CD8 T cells/mg vs. 4.1 ± 3.1 CD8 T cells/mg, respectively) (Extended Data Fig 2A). Among skin-infiltrating CD8 T cells, GP33 (Ag)-specific cells were undetectable in negative control mice but were present in both Ag ON (0.2 ± 0.08%; 1 ± 1 cells/mg) and Ag ON/CPI (2 ± 1%; 15 ± 11 cells/mg) samples (Extended Data Fig 2B,C). In line with this, depletion of CD8 T cells alone or in combination with CD4 T cells led to significantly decreased median pathological scores in Ag ON/CPI mice (7.5 or 15 vs. 90, respectively), while depletion of CD4 T cells alone did not (140 vs. 90; Fig 2B and Supplementary Fig 1). Moreover, the pathological scores of CD8 or CD4/8 T cell-depleted Ag ON/CPI mice were not statistically different from those of Ag ON mice (median = 2.5, Fig 2B).

To define the CD8 T cell-dependent mechanism of cutaneous disease in Ag ON/CPI mice, we utilized N/C mice adoptively transferred with naïve Thy1.1/1.1+ dsRED- or firefly Luciferase (fLuc)-expressing GP33-specific CD8 T cells from TCR transgenic P14 mice[26] (referred to as P14 CD8 T cells). We confirmed that presence of P14 CD8 T cells did not alter the phenotypes observed in Ag ON and Ag ON/CPI mice (Supplementary Fig 2). fLuc-expressing P14 CD8 T cells were imaged by IVIS and became detectable 2 days after starting Dox/4-OH-Tam treatment only in Ag-expressing mice (Fig 2C). By day 5, the fLuc signal was present in Ag ON and Ag ON/CPI mice, likely in inguinal lymph nodes (draining the Ag-expressing skin area, dLNs) and spleen, but not in Ag-expressing skin (Fig 2C). However, by day 10, the fLuc signal was detected in the skin of Ag ON and Ag ON/CPI mice and was largely restricted to the Ag-expressing areas (Fig 2C). While the fLuc signal measured at day 10 in the Ag-expressing skin area of Ag ON/CPI mice was higher than in Ag ON mice (average radiance of day 10 ROIs shown in Fig 2C = $3 * 10^5 \pm 1 * 10^5$ photons/sec/cm2/sr vs. $7 * 10^4 \pm 2 * 10^4$ photons/sec/cm2/sr, Fig 2D), both Ag ON and Ag ON/CPI mice had early and sustained skin infiltration by Ag-specific CD8 T cells, suggesting that the cutaneous disease score differences between Ag ON and Ag ON/CPI mice were not simply the result of a kinetic difference of skin infiltration by the Ag-specific CD8 T cells. Of note, Ag-specific P14 CD8 T cells persisted in Ag-expressing skin for up to 31 days after initiating Dox/4-OH-Tam treatment without causing overt cutaneous disease (Extended Data Fig 3A–F).

Confocal microscopy analysis of Ag-expressing skin at experimental endpoint (day 15) confirmed presence of dsRED+ P14 CD8 T cells in both Ag ON and Ag ON/CPI mice and showed that P14 CD8 T cells were mostly localized in the dermis in Ag ON mice, while infiltrating the epidermis in Ag ON/CPI mice (Fig 2E). In line with this, development of localized cutaneous disease in N/C mice was associated with CD8 T cell-dependent loss of Ag-expressing cells (mostly EpCAM+CD45- keratinocytes) in the 4-OH-Tam-treated skin area in Ag ON/CPI mice vs. Ag ON mice (10 ± 7% vs. 23 ± 6% of total skin cells, Fig 2F,G and Supplementary Fig 3).

PD-1 controls CD8 T cell location

In the presence of skin-specific Ag expression, skin-infiltrating Ag-specific CD8 T cells upregulated surface expression of PD-1 (MFI = 6013 ± 636 and 2196 ± 1042 in Ag ON and Ag ON/CPI mice, respectively) and CTLA-4 (MFI = 2038 ± 203 and 1472 ± 81 in Ag ON and Ag ON/CPI mice, respectively, Fig 3A). Following the same experimental schedule shown in Supplementary Fig 2A, we then compared the outcome of single-agent blockade in Ag-expressing mice. PD-1 blockade alone was sufficient to cause moderate-to-severe cutaneous disease (pathological scores 30–160, median = 105), but blockade of CTLA-4 as a single agent was not (pathological scores 0–90, median = 25) (Fig 3B). Of note, the cutaneous disease developed in Ag ON/CPI mice receiving single blockade of PD-1 appeared less severe than in Ag ON/CPI mice treated with dual blockade of PD-1/CTLA-4 (median = 145), although differences were not statistically significant (Fig 3B).

To test if PD-1-mediated regulation acted intrinsically to Ag-specific CD8 T cells to prevent cutaneous pathology in our model, we used the CRISPR/Cas9 technology to knock out PD-1 in naïve Thy1.1+dsRED+ P14 CD8 T cells prior to adoptive transfer into N/C recipients (Supplementary Fig 4). Following skin-specific Ag induction, both PD-1 KO and mock-edited PD-1 wt P14 CD8 T cells infiltrated the Ag-expressing skin area (0.3 ± 0.1% and 23 ± 11% of total skin cells, respectively, Fig 3C), however, while mice receiving PD-1 wt P14 CD8 T cells (“Ag ON/PD-1 wt” mice) had pathological scores ranging 0–200 with 55% of mice displaying normal skin or mild cutaneous pathology in Ag-expressing skin (overall median = 10), 100% of mice receiving PD-1 KO P14 CD8 T cells (“Ag ON/PD-1 KO” mice) developed moderate-to-severe cutaneous pathology in the Ag-expressing skin area (pathological scores 30–215, median = 110) (Fig 3D). Cutaneous pathology was associated with significant loss of Ag-expressing skin cells in Ag ON/PD-1 KO mice compared to Ag ON/PD-1 wt mice (1 ± 0.5% and 15 ± 13% of total skin cells, respectively, Fig 3E), in line with consistent epidermal infiltration by the PD-1 KO P14 CD8 T cells (Fig 3F).

Because P14 CD8 T cells were already primed and expanding by day 5 after initiating Dox/4-OH-Tam treatment (Fig 2C), we next tested whether skin pathology would develop if PD-1 blockade was initiated 5 days after beginning Dox/4-OH-Tam treatment (Extended Data Fig 3G). Delayed PD-1 blockade (day 5) led to cutaneous pathology that was comparable to mice receiving Dox/4-OH-Tam and PD-1 blockade concomitantly (day 0) (Extended Data Fig 3H), suggesting that PD-1 regulates CD8 T cell pathogenicity independent of priming by DCs. Together, our data suggest that PD-1 maintains skin tolerance in our model by preventing Ag-specific CD8 T cells from accessing Ag-expressing cells in the epidermis.

Skin cellular makeup after Ag +/− CPIs

We next assessed transcriptomic differences at experimental endpoint (day 15) between Ag OFF, Ag ON, and Ag ON/CPI skin using single-cell RNA sequencing (scRNAseq) (Supplementary Fig 5). Based on analysis with UMAP, our skin samples contained epithelial cells, fibroblasts, myeloid cells, and T cells (Extended Data Fig 4A,B), however the fraction of epithelial cells was particularly decreased in Ag ON/CPI mice (representing 67%, 46% and 18% of all cells in Ag OFF, Ag ON and Ag ON/CPI mice, respectively) while the

fraction of both T cells (25% vs. 40% and 67%, respectively) and myeloid cells (5% vs. 12% and 14%, respectively) were increased in Ag ON and Ag ON/CPI mice compared to Ag OFF mice (Extended Data Fig 4C,D). These differences were corroborated by analyzing our scRNAseq dataset with PHATE[27] (Extended Data Fig 4E,F). Further analysis showed that Ag induction decreased the fraction of γδ T cells and increased αβ T cells in skin (particularly *Dsred*-expressing P14 CD8 T cells), and this was exacerbated by CPI treatment (Extended Data Fig 4G–K). Thus, in line with our flow cytometric findings, substantial changes in the cellular makeup of the skin following Ag induction and CPI treatment were confirmed at the transcriptional level.

Local CD8 T/myeloid cell interactions

The cellular changes observed in Ag ON mice suggested that tolerance in skin could be associated with local events of tissue remodeling. This was exemplified by the quantitative and qualitative changes in local myeloid cells following skin-specific Ag expression. Ag-induction led to local decreases in Langerhans cells (*Epcam*/*Cd207*-expressing cells) and increases in CD11b+CD11c+CD16+ macrophages (*Itgam*/*Itgax*/*Cd16*-expressing cells) and CD11b-CD11c+ DCs (*Itgax*-expressing cells), and this was enhanced by CPI treatment (Fig 4A,B and Extended Data Fig 5A–C). Using flow cytometry, we observed a ~10-fold increase in the frequency of CD11b+CD11c+CD16+ cells between Ag OFF (0.6 ± 0.1% of CD45+EpCAM- cells) and Ag ON (5 ± 2%) or Ag ON/CPI (6 ± 2%) mice (Fig 4C and Extended Data Fig 5D), and this increase was CD8 T cell-dependent (Fig 4C). The CD11b+CD11c+CD16+ cells that infiltrated skin upon local Ag expression had surface expression of MHC-I (H2Db), PD-L1, CD80, and CD86, and these changes were also CD8 T cell-dependent (Fig 4D and Extended Data Fig 5D). MHC-I and PD-L1 are upregulated by IFNγ signaling[28]. In Ag-expressing mice, CD8 T cells were the only *Ifng*-expressing skin population (Extended Data Fig 5E,F), while CD11b+CD11c+CD16+ cells expressed both *Ifngr1* and *Ifngr2* and downstream IFNγ target genes (*Stat1*, *Irf1*, *Ifitm1*, *Ifit1*, and *Ifit2;* Extended Data Fig 5G). Expression of Type I and III IFNs was not detected in any cell (data not shown).

Confocal microscopy showed accumulation of CD11b+ cells in the dermis of Ag-expressing mice, where most Ag-specific CD8 T cells were found in the Ag ON condition (Fig 4E and Fig 2E). Using the CellPhoneDB algorithm[29], we assessed the cell-cell interactions in the skin of Ag OFF, Ag ON, and Ag ON/CPI mice. The most numerous and significant ligand/receptor pairs expressed in both Ag ON and Ag ON/CPI mice were in myeloid cells and T cells (Supplementary Fig 6). These included chemokines *Cxcl9*, *Cxcl10, Cxcl16* and their receptors *Cxcr3* and *Cxcr6* expressed by myeloid cells and T cells, respectively, chemokines *Ccl3*, *Ccl4*, *Ccl5* and their receptors *Ccr1* and *Ccr5* expressed by both myeloid cells and T cells, the macrophage migration inhibitory factor *MIF* and its receptor *Cd74* expressed by T cells and myeloid cells, respectively, and checkpoint receptors *Pdcd1, Havcr2*, *Cd47* and their ligands *Cd274*, *Pdcd1lg2*, *Lgals9* expressed by T cells and myeloid cells, respectively (Extended Data Fig 6A,B). Thus, our analysis showed that, under conditions of skin tolerance, local infiltration of Ag-specific CD8 T cells led to changes in myeloid cell populations and revealed a complex network of potentially redundant signals that could mediate interactions between Ag-specific CD8 T cells and myeloid cells.

CPIs unleash CD8 T cell pathogenicity

Given the visible differences between Ag ON and Ag ON/CPI mice, we asked if CPIs directly affected the functional state of skin-infiltrating Ag-specific CD8 T cells. We hypothesized two models of how checkpoint receptors maintained Ag-specific CD8 T cell tolerance in skin: a bifurcated model, in which presence of checkpoint receptors drives T cell differentiation towards a tolerant state and absence of checkpoint receptors leads to a T cell pathogenic state; or a linear model, where checkpoint receptors alter the degree to which CD8 T cells differentiate along a common pathway, with the tolerant and pathogenic states being different, but consecutive, states along the differentiation trajectory (Fig 5A). Based on previous literature[5–14], we initially favored the idea that T cells in the N/C model would follow a bifurcated differentiation trajectory. To assess this, we analyzed differential gene expression between skin-infiltrating P14 CD8 T cells in Ag ON and Ag ON/CPI mice (Fig 5B and Extended Data Fig 7A). Surprisingly, this analysis indicated that Ag-specific CD8 T cells in these conditions had comparable transcriptional profiles (Fig 5C), characterized by the expression of genes associated with T cell activation and effector function (for example, *Gzma*, *Gzmb*, *Ifng*, *Cd28*, *Ccl3*, *Ccl5*; Fig 5D and Extended Data Fig 7B). T cell checkpoint receptors (*Pdcd1*, *Havcr2*, *Lag3* and *Tigit*) were also similarly expressed in Ag ON and Ag ON/CPI mice (Fig 5D and Extended Data Fig 7B). Very few genes appeared differentially expressed between these two conditions, specifically *Gzma*, *Ifitm1* and *Ifitm2*, *Ly6e*, *Itgae*, *Il7r, Ccl3,* and *Ifi27l2a* (Fig 5C). Notably, Ag-specific CD8 T cells in Ag ON/CPI mice upregulated *Itgae* (CD103), which is consistent with their epidermal localization [30] (Fig 5C,D). However, the lack of significant difference in *Ifng* and *Tnf* expression was particularly striking, as we found that skin-infiltrating P14 CD8 T cells from Ag ON/CPI mice produced and secreted higher amounts of these proteins compared to Ag ON mice following *ex vivo* Ag stimulation and flow cytometric analysis (Fig 5E,F). This evidence suggested that some differences in key effector functions of the Ag-specific CD8 T cells from Ag ON and Ag ON/CPI mice were the consequence of post-transcriptional regulation.

Despite the transcriptional similarities, MELD analysis[31] was used to quantify the likelihood of finding P14 CD8 T cells in each one of the experimental conditions (Fig 5G and Extended Data Fig 7C), and this analysis suggested a population shift in Ag ON/CPI mice. To investigate this, we defined the differentiation trajectories of the skin-infiltrating P14 CD8 T cells from Ag ON and Ag ON/CPI mice using pseudotime analysis (Fig 5H and Extended Data Fig 7D,E). In both conditions, P14 CD8 T cells were largely in “later” pseudotime (0.5–1), with most cells between 0.9 and 1. By following the normalized expression of several effector genes across pseudotime, we found that similar changes in expression were observed as T cells increased in pseudotime between the Ag ON and Ag ON/CPI conditions (Extended Data Fig 7F). However, CPI treatment resulted in a further shift of the P14 CD8 T cell population towards the more differentiated end of the pseudotime spectrum (1), indicating that the observed increases in expression for genes like *Gzma, Ifitm1*, *Ifitm2*, *Ly6e*, *Itgae*, and *Il7r* were due to a higher proportion of cells reaching the late stage of differentiation where these genes were upregulated, and not due to a bifurcated differentiation trajectory. To test this finding with an alternative method, we compared the transcriptional profiles of P14 CD8 T cells from Ag ON and Ag ON/CPI

mice to GP33-specific CD8 T cells from mice infected with LCMV-Clone13 (day 28 post infection), which do undergo a bifurcated differentiation process[32], and from mice infected with LCMV-Armstrong (day 28 post infection), which instead undergo a linear differentiation process[33] (Extended Data Fig 8A–C). Unlike in LCMV-Clone13 infection, where stem-like GP33-specific CD8 T cells differentiate into either effector or exhausted cells, the tolerant (Ag ON) and pathogenic (Ag ON/CPI) GP33-specific CD8 T cells were in a single overlapping cluster (note the projecting "tail" composed of proliferating T cells), more in line with the linear memory precursor-to-terminal effector cell differentiation seen following LCMV-Armstrong infection. Thus, our data were consistent with peripheral CD8 T cell tolerance in skin being mediated via a linear differentiation process, where checkpoint receptors prevent Ag-specific CD8 T cells from reaching a fully differentiated, pathogenic state.

N/C mice model cutaneous lichenoid irAEs

The macroscopic appearance of the cutaneous disease in Ag ON/CPI mice was reminiscent of cutaneous lichenoid irAEs that are found in patients after CPI immunotherapy, particularly with PD-1/PD-L1 blockade (Fig 6A)[17,34]. For example, both Ag ON/CPI mice and patients with lichenoid irAEs presented with scaled crust, reticular scales and papules at the macroscopic level (Fig 6B) and necrotic keratinocytes, spongiosis and lymphocytic accumulation at the dermis/epidermis interface at the microscopic level (Fig 6C).

By scRNAseq analysis of punch biopsies from matched affected (lesional) and normal (non-lesional) skin from two patients with confirmed diagnoses of lichenoid irAE and three healthy donors (Extended Data Fig 9 and Supplementary Table 1) we identified a cluster of CD8 T cells (Cluster 1) in both lesional and non-lesional skin characterized by expression of genes coding for T cell effector molecules (*Gzma*, *Gzmb*, *Ifng*, and *Tnf*) and activation genes (*Cd28*, *Mki67*, *Itgae, Ccl3*, and *Ccl5*), as well as checkpoint receptor-coding genes (*Pdcd1*, *Lag3* and *Tigit*) (Fig 6D, Extended Data Fig 10A–H, and Supplementary Table 2), consistent with recent findings in cutaneous irAEs[20]. Moreover, scatterplot analysis showed that the gene expression profiles of Cluster 1 cells in lesional and non-lesional skin were comparable (Fig 6E; Supplementary Table 3). These data indicated that the N/C model of cutaneous immunopathology is faithful to many of the features of CPI-dependent lichenoid irAEs in humans. Moreover, our analyses showed that, similarly to the N/C model, CD8 T cells with effector capacity existed in both normal and diseased human skin from lichenoid irAE patients and that these cells were transcriptionally similar in the two conditions.

Paired V(D)J sequencing of lesional and non-lesional skin samples identified 740 cells expressing *TRAV/TRBV* sequences shared by at least two cells, for a total of 258 different clones (Extended Data Fig 10I,J and Supplementary Table 4). Of these clones, 14 were found in healthy donor skin, while the remaining 244 were sequenced in lesional and/or non-lesional skin and had sizes ranging from 2 to 30 cells (Supplementary Table 4). Lesional skin was infiltrated by numerous expanded T cell clones. The four biggest clones found in this sample were composed by more than 10 cells and included CD8 T cells from Cluster 1 exclusively (Fig 6F). Clones of non-cytotoxic CD8 T cells (Clusters 2–5) were also found in lesional skin, but these clones were smaller (2–10 cells) and often contained

cells from at least two different clusters (Extended Data Fig 10J). Of note, non-lesional skin also contained some expanded clones of Cluster 1 CD8 T cells, the biggest of which was composed of 6 cells (Fig 6F). Two expanded clones of Cluster 1 CD8 T cells were found in both lesional and non-lesional skin, and one of these clones was significantly expanded in lesional vs. non-lesional skin (15 vs 3 cells, respectively; Fig 6F). Together, our findings suggests that CD8 T cells are likely involved in the pathogenesis of cutaneous lichenoid irAEs and are consistent with a model of peripheral tolerance in skin where human skin-infiltrating CD8 T cells with effector properties are restricted from causing local pathology due to PD-1 function.

Discussion

The peripheral T cell repertoire in healthy humans contains naïve self-Ag-specific CD8 T cells with frequencies and TCR affinities similar to those of pathogen-specific T cells[1,2], thus suggesting a critical role for peripheral T cell tolerance mechanisms in maintaining immune homeostasis[22]. Numerous studies have pointed at the pruning of potentially pathogenic CD8 T cells from the peripheral repertoire via clonal deletion and anergy as key mechanisms of peripheral T cell tolerance[4–6,9–12]. However, self-Ag-specific T cells have been shown to escape peripheral tolerance[35] and thus the question remains as to how immunopathology is avoided in immunologically healthy individuals.

Checkpoint receptors have been linked to the induction of peripheral CD8 T cell tolerance via clonal deletion and anergy[7,9–14]. However, under physiologic conditions, it remains uncertain if immune checkpoint receptors also maintain self-reactive CD8 T cells in a tolerant state. The high frequency of irAEs in patients receiving CPI immunotherapy[15] led us to hypothesize that peripheral self-Ag-specific CD8 T cells could be held in a non-pathogenic (tolerant) state by checkpoint receptors, thus maintaining immune homeostasis.

In the N/C model, skin-infiltrating CD8 T cells specific for a locally expressed Ag had a transcriptional signature of effector T cells, yet they co-existed in skin with cells expressing their cognate Ag for up to 30 days. This state of tolerance was maintained thanks to the function of the checkpoint receptor PD-1 and was distinct from the anergic states described in classical experimental models of peripheral tolerance, where T cells never acquired effector functions (like Granzyme B expression) or infiltrated Ag-expressing tissues [4–6,9–14]. Instead, our data support a linear differentiation model under homeostatic conditions in which checkpoint receptors maintain local CD8 T cell tolerance and prevent skin pathology by (1) preventing most Ag-specific effector CD8 T cells from reaching a fully differentiated, highly pathogenic state, (2) limiting effector capacity at the post-transcriptional level, possibly due to metabolic regulation[36], and (3) restricting the access of Ag-specific CD8 T cells to the epidermis, where Ag-expressing cells are located. Tolerant CD8 T cells in Ag ON mice were largely restricted to the dermis, in line with a role for PD-1/PD-L1 interactions in restricting T cell motility[37] and interfering with Ag recognition[38]. Interactions between skin-infiltrating Ag-specific CD8 T cells and CD11b+CD11c+CD16+ macrophages in the dermis could help maintain T cells tolerant and physically separated from Ag-expressing epidermal cells, as myeloid cells have been previously shown to control localization and maintenance of CD8 T cells in skin, especially via the CXCL16/

CXCR6 axis[39]. Thus, while *de novo* Ag expression in the skin of N/C mice promoted the differentiation of effector CD8 T cells, peripheral tolerance could still be maintained by the function of checkpoint receptors and via interactions between CD8 T cells and myeloid cells.

The mechanisms by which CPIs caused loss of tolerance towards skin-expressed Ags appeared different from the mechanisms by which CPI immunotherapy boosts T cell responses in chronic viral infection and cancer. In cancer, for example, tumor-infiltrating stem-like precursor CD8 T cells are required for CPI therapeutic effectiveness [40]. In this context, stem-like precursor CD8 T cells undergo bifurcated differentiation into an exhausted or an effector state and CPI immunotherapy is thought to promote the latter [41]. However, when we conducted an integrated scRNAseq analysis of GP33-specific CD8 T cells from different experimental settings, we noted that, unlike GP33-specific CD8 T cells undergoing exhaustion, tolerant GP33-specific CD8 T cells from the skin of N/C mice did not contain stem-like cells. This observation also suggests fundamental biological differences between the process of T cell tolerogenesis in skin and the process of T cell exhaustion.

In conclusion, our data support the hypothesis that checkpoint receptors like PD-1 function as gatekeepers of tissue homeostasis by allowing the presence of functional T cells in peripheral tissues without immunopathology. We speculate that CPI immunotherapy may interfere with these local regulatory networks, thus resulting in irAEs. Future studies will be focused on understanding how and where naïve skin Ag-specific CD8 T cells become tolerant, as both clinical [42] and experimental [43–45] evidence has shown that checkpoint receptor-mediated regulation of T cells may occur at multiple anatomical sites.

Methods

Mouse studies

All studies were carried out in accordance with the guidelines of the Declaration of Helsinki and approved by the Institutional Animal Care and Use Committees of Yale University (IACUC #2022_20112). All mice were bred in specific pathogen-free conditions. 6–12 week old female and male mice with the correct genotype were randomly allocated to experimental groups. The minimum sample size was chosen to reach statistical significance compared to control mice.

Human samples

For histological analysis, cases of lichenoid cutaneous irAEs were identified by searching the Yale Dermatopathology clinical case database. Selected cases were de-identified and H&E-stained slides from clinical biopsy samples were imaged. These studies were conducted according to the guidelines of the Declaration of Helsinki and approved by the Yale Institutional Review Board (IRB protocol #1501015235).

For scRNAseq analysis (see details below), 4mm skin punch biopsies were obtained from lesional and non-lesional (back) skin from two patients with active lichenoid irAE occurring while undergoing treatment with PD-1 inhibitors. The diagnosis of lichenoid irAE was

confirmed by the patients' primary dermatologist. Both patients were treating their eruptions with topical triamcinolone 0.1% ointment at the time of biopsy. Additionally, three healthy donors were recruited to obtain control skin punch biopsies (also back). The study was conducted according to the guidelines of the Declaration of Helsinki and was approved by the Yale Institutional Review Board (IRB protocol #2000027571), and all patients and healthy donors were consented. To obtain single cell suspensions, biopsy specimens were incubated in 1% Dispase II (Sigma-Aldrich, cat. D4693) in RPMI with 10% FBS for 45min at 37°C, followed by mincing with scalpel, incubation in 0.05% Liberase TL (Sigma-Aldrich, 05401020001) in RPMI with 10% FBS and 0.008% DNase I (Roche, cat. 10104159001) for 45min at 37°C, and then straining through 40μm mesh.

Mouse strains and genotyping

C57BL/6J (B6) mice were purchased from JAX (stock # 000664) and bred in house. NINJA mice were generated as previously described [23]. NINJA x CAG-rtTA3 were generated by crossing NINJA mice to CAG-rtTA3 mice (JAX, stock # 016532) and are henceforth referred to as NINJA. N/C (*Rosa26-NINJA/CreER^{T2};CAG-rtTA3 Tg*) mice were generated by crossing NINJA mice to R26-CreER^{T2} mice (JAX, stock # 008463). Thy1.1/1.1+ fLuciferase- or dsRED-expressing TCR transgenic P14 mice were generated in house by crossing Thy1.1/1.1+ P14 mice [26] to fLuciferase-expressing mice (JAX, stock #025854) or dsRED-expressing mice (JAX, stock #006051). For genotyping, mouse tail DNA was amplified using GoTaq G2 Green Master Mix (Promega, cat. M7823) or KAPA Taq PCR Kit (Takara Bio, cat. R040A). Primers Rosa26 WT F, Rosa26 WT R, and Rosa26 Ninja R (Supplementary Figure 7) were used for genotyping of the NINJA allele, with expected bands of 378bp for WT allele and 280 bp for NINJA allele. For CAG-rtTA3 genotyping, primers CAGrtTA common F, CAGrtTA WT R and CAGrtTA Transgene R (Supplementary Figure 7) were used and expected bands were 360bp for WT allele and 330bp for Transgene. For R26-CreER^{T2} genotyping, primers generic-Cre_1, generic-Cre_2, generic-Cre_3 and generic-Cre_4 (Supplementary Figure 7) were used with expected bands of 500bp for internal control and 320bp for Transgene. For P14 genotyping, primers P14r F and P14r R (Supplementary Figure 7) were used with expected band of 300 bp for Transgene. For fLuciferase genotyping, primers 10946, 10947, oIMR7338 and oIMR7339 (Supplementary Figure 7) were used with expected bands of 324bp for internal control and 200bp for Transgene. For dsRED genotyping, primers oIMR3847, oIMR4110, oIMR7338 and oIMR7339 (Supplementary Figure 7) were used and expected bands were 324bp for internal control and 208bp for Transgene.

In vivo *induction of NINJA antigens in the skin and antibody treatments*

Mice were fed Dox-containing food (Envigo Teklad, cat. TD.120769) for ten consecutive days. Mice also received four doses of a 50mg/mL solution of 4-OH-Tam (Millipore Sigma, cat. T176) in DMSO (AmericanBIO, cat. AB03091) that was painted on the indicated area of the skin on the lower back of each experimental mouse (20–30uL/dose) every other day starting the day after addition of Dox diet.

For CPI treatment, PD-1 blocking antibody (clone 29F.1A12) and CTLA-4 blocking antibody (clone 9D9) were administered either in combination or as single agents at 100ug/antibody/mouse every third day starting on the day of Dox diet addition for four total doses.

For T cell depletion, CD8 depleting antibody (clone 53–6.7) and CD4 depleting antibody (clone GK1.5) were administered either in combination or as single agents at 200ug/antibody/mouse every third day starting one week prior to Dox diet addition for seven total doses. Detailed information on antibodies is provided in the Reporting Summary.

Knock-out of PD-1 in P14 CD8 T cells

Naïve dsRED+ P14 CD8 T cells were isolated from spleen using the EasySep CD8 T cell negative selection kit (STEMCELL Technologies, cat. 19853) according to manufacturer's instructions. Gene editing protocol was adapted from[46]. Briefly, Cas9/sgRNA ribonucleoproteins (RNPs) were formed by mixing PD-1-targeting (5'-GACACACGGCGCAAUGACAG-3') or non-targeting control sgRNA (5'-GCACUACCAGAGCUAACUCA-3') (CRISPRevolution sgRNA EZ Kit, Synthego) with Cas9 nuclease V3 (IDT, cat. 1081059). 5–10 * 10^6 dsRED+ P14 CD8 T cells were mixed with Cas9/sgRNA RNPs and electroporated with the Lonza P3 Primary Cell 4D-Nucleofector X kit (cat. V4XP-3032) according to manufacturer's instructions. 10^5 electroporated dsRED+ P14 CD8 T cells were then transferred into N/C recipients by retro-orbital injection (I.V.) one day prior to initiating Dox/4-OH-Tam regimen for skin-specific Ag induction. Leftover electroporated P14 CD8 T cells were used to extract genomic DNA (DNeasy Blood & Tissue kit, Qiagen, cat. 69504) or were restimulated *in vitro* with hIL-2 (PeproTech, cat. 200–02) and anti-CD3/CD28 Dynabeads (ThermoFisher Scientific, cat. 11452D) to confirm PD-1 knock-out by Sanger sequencing and flow cytometry, respectively.

LCMV infections

B6 mice were infected with LCMV-Armstrong at 2 * 10^5 pfu/mouse I.P. or LCMV-Clone13 at 4 * 10^6 pfu/mouse I.V. Mice were euthanized 8 or 28 days after infection to collect spleens. Both LCMV-Armstrong and LCMV-Clone13 were produced in house.

Preparation of skin, LN cells, and spleen cells, in vitro *antigen-specific restimulation and flow cytometry*

4-OH-Tam-treated skin was harvested at experimental endpoint and processed using the mouse epidermis dissociation kit according to manufacturer's instructions (Miltenyi, cat. 130–095-928). LN and spleen cells were harvested and processed as previously described [23].

For Ag-specific restimulation, 1 * 10^6 cells from skin were cultured for 6hr at 37°C in 5% CO_2 in complete RPMI-1640 (10% HI-FBS, 55μM beta-mercaptoethanol, 1x Pen/Strep and 1x L-Glut) supplemented with LCMV $GP_{33–41}$ peptide (0.5μg/mL, AnaSpec, cat. AS-61296) or left unstimulated in the presence of 10^4 wild-type congenically marked donor LN Ag-presenting cells.

For flow cytometric analysis or FACS, 1–5 * 10^6 cells were stained with 1:300 dilutions of antibodies specific for surface markers Thy1.2 (30-H12), Thy1.1 (OX-7), CD8α (53–6.7),

CD8β (53–5.8), CD4 (GK1.5 or RM4–4), CD44 (IM7), PD-1 (29F.1A12), CTLA-4 (UC10–4B9), EpCAM (G8.8), CD45 (30-F11), CD11b (M1/70), CD11c (N418), PD-L1 (10F.9G2), and CD107a (1D4B). Tetramers for H2Db/$GP_{33–41}$-specific CD8 T cells were obtained from the NIH Tetramer Core Facility. For intracellular staining, cells were processed using the Fixation/Permeabilization kit from BD Biosciences (BD Cytofix/Cytoperm, cat. 554714) following manufacturer's instructions and stained with 1:200 dilutions of antibodies specific for GrzA (3G8.5), GrzB (GB11), IFNγ (XMG1.2) and TNFα (MP6-XT22). Detailed information is provided in the Reporting Summary. Samples were analyzed on a BD Biosciences Symphony A5 flow cytometer or sorted on a BD Biosciences FACSAria flow cytometer using BD Biosciences FACSDiva software v6.1.3.

In vivo *imaging by IVIS*

Hair was removed from back of mice and mice were adoptively transferred with 5×10^3 fLuc+ P14 T cells by retro-orbital injection (I.V.) one day prior to initiating Dox/4-OH-Tam regimen. Two, five, ten, fourteen, twenty-five or thirty days later mice were injected I.V. with a PBS solution containing 3mg of luciferin/mouse (XenoLight D-Luciferin - K+ Salt, PerkinElmer, cat. 122799) and imaged using an *In Vivo* Imaging system instrument with Living Image Software v4.7.3 (IVIS, PerkinElmer).

IF/IHC

For adoptive transfer experiments, mice were adoptively transferred with 5×10^3 dsRED+ P14 T cells by retro-orbital injection (I.V.) one day prior to initiating Dox/4-OH-Tam regimen. Mice were euthanized at experimental endpoint to collect 4-OH-Tam-treated skin.

For IF, tissue was fixed overnight at 4°C with a paraformaldehyde-lysine-periodate fixative (PLP), subsequently cryoprotected with 30% sucrose in PBS for 6–8hr at 4°C, and then embedded in cryomolds with 100% optimum cutting temperature (O.C.T.) compound (VWR, cat. 25608–930) on dry ice for freezing. Tissue sections were stained with 1:200 dilutions of primary antibodies specific for CD3e (SP7), CD8β (YTS156.7.7), CD11b (M1/70), Keratin-10 (DE-K10) or Thy1.1 (OX-7) followed by staining with 1:200 dilutions of AF488 goat-anti rabbit, AF647 goat anti-rat, or AF594 goat anti-mouse secondary antibodies as previously described [23] and processed with Vectashield Antifade mounting medium with DAPI (Vector Laboratories, cat. H-1200–10). Imaging was performed on a Leica SP5 confocal microscope with LAS X LS software (Leica).

For IHC, skin tissues were fixed in a 1x formaldehyde solution in PBS (Millipore-Sigma, cat. 252549) and then embedded in paraffin and sectioned by the Yale School of Medicine Comparative Pathology Research Core. All skin tissues were processed and stained with H&E or with 1:200 dilutions of primary antibodies specific for CD3e (clone SP7) or dsRED (polyclonal) followed by staining with a 1:200 dilution of HRP goat anti-rabbit secondary antibody as previously described [23]. Detailed information is provided in the Reporting Summary. Imaging of IHC samples was performed using an EVOS Imaging System with EVOS M5000 software (ThermoFisher Scientific).

Epidermal thickness score calculation

H&E-stained slides were obtained and imaged from each experimental sample as described above. Three independent ROIs were considered in each H&E image from various locations along the epidermis. Epidermal thickness was then calculated within each ROI by The Histological Inflammation Computation (THIC) analysis in MATLAB vR2020b. Briefly, the pixel area and perimeter of each ROI were defined by the total number of white pixels and the boundary length of the observed binary epidermis. For each ROI, epidermis thickness in μm was calculated by dividing the ROI area by the perimeter. MATLAB code for initializing the THIC GUI and project files are available to use for research purposes only at https://github.com/dakwok/The-Histological-Inflammation-Computation-software.

Cutaneous pathological severity scoring calculation

Experimental mice were scored blindly. The scoring method is based on the Lichen Planus Severity Index [25]. Briefly, each pathological score is calculated at experimental endpoint by assigning weights to the various morphologies of skin pathology: erythema (weight = 1), scale (weight = 1), lichenification (weight = 2), and erosion/ulceration (weight = 4). For each morphology seen in a given experimental mouse, the weight of that morphology is multiplied by the percentage of “at-risk” skin involved, defined as the area treated with topical 4-OH-Tam. These products are calculated for each morphology of lesion, and the results are summed, giving the final pathological score.

Single-cell RNA sequencing

For Ag OFF, Ag ON and Ag ON/CPI samples, NINJA and N/C mice were adoptively transferred with 5×10^3 dsRED+ P14 T cells by retro-orbital injection (I.V.) one day prior to initiating Dox/4-OH-Tam regimen. Mice were euthanized at experimental endpoint to collect 4-OH-Tam-treated skin, which was processed as described above.

For human skin samples, biopsies were collected and processed as described above.

For LCMV-infected samples, Thy1.2+CD8+CD4-GP33tetramer+ cells were isolated by FACS 28 days post infection from the spleen of B6 mice infected with either LCMV-Armstrong or LCMV-Clone13 as described above.

scRNAseq libraries were prepared by the Yale Center for Genome Analysis using Chromium Single Cell 5’ Reagent Kit (10X Genomics), according to manufacturer’s instructions, and sequencing was performed on an Illumina NovaSeq 6000 system with NovaSeq Control Software v1.7.5.

For mouse skin sample analysis, scRNAseq datasets were processed with CellRanger v3.1.0 using the mm10 mouse genome indices from 10X Genomics. Libraries were further preprocessed in Python v3.10 using the scprep package (https://github.com/krishnaswamylab/scprep), removing cells with library size lower than 1500 unique molecular identifiers (UMI) per cell and more than 15000 UMI per cell. Cells with high mitochondrial content (>85th percentile per sample) were removed, and genes not detected in any of the six samples were removed. The resulting data matrix was then normalized by library size to 1,000 counts per cell and log-transformed. After the above filtering, there

were 21,178 cells and 21,515 genes used for all downstream analysis. This corresponds to 8,167 cells from Ag ON samples; 3,944 cells from Ag ON/CPI samples; and 9,067 cells from Ag OFF samples. For visualization, we embedded the cells based on similarity in transcriptional profiles using PHATE [27] or UMAP with knn=40 and decay=10. We clustered the cells using spectral clustering of the cellular graph, and we annotated clusters based on marker expression. After annotation, our dataset consisted of 8,196 T cells; 10,521 epithelial cells; 2,008 myeloid cells; and 453 fibroblasts. To characterize differences across conditions, we leveraged MELD [31] which, for each cell, quantifies the likelihood that it was affected by the experimental condition. This provides a continuous measure of the effect of each condition across the transcriptomic space, and aids in visualization of the experimental response. To visualize gene expression, we imputed missing and dropped-out values with MAGIC [47].

To compare differentiation trajectories for Ag-specific CD8 T cells in Ag ON and Ag ON/CPI conditions, we first built a cell graph for each condition and defined pseudotime as the Fiedler vector of the graph. As the majority of cells resided in the later part of the trajectory, we compared gene expression for several markers over pseudotime between 0.5 and 1. Expression counts were smoothed with MAGIC and z-score normalized for direct comparison.

For cell-cell communication analysis, we used an efficient reimplementation of the CellPhoneDB algorithm and the CellPhoneDB repository of ligand (L)-receptor (R) interactions [29]. CellPhoneDB predicts R-L interactions between two cell types based on expression of a R by one cell type and a L by another cell type. Rs and Ls expressed specifically and robustly in each cell type are considered enriched, and enrichment is computed based on a random permutation test of cell type labels. To compare interactions between conditions for myeloid -> T cell interactions, we calculated the Pearson correlation of each L expression with the sample likelihood in myeloid cells, and the Pearson correlation of each R expression with the sample likelihood in T cells. For each L-R pair, we took the mean ligand and receptor correlation to summarize the interaction association.

The LCMV scRNAseq datasets were processed with CellRanger v5.0.0 using the mm10 mouse genome indices from 10X Genomics. Libraries were further preprocessed in Python v3.10 using the scprep package (https://github.com/krishnaswamylab/scprep), retaining cells with library size between 15th and 85th percentile. Cells with high mitochondrial content (>85th percentile per sample) were removed, and genes not detected in either the LCMV-Armstrong or the LCMV-Clone13 sample were removed. The resulting data matrix was then normalized by library size to 1,000 counts per cell and log-transformed. After filtering, there were 7,853 cells and 15,660 genes. This corresponds to 7,056 cells from the LCMV-Armstrong sample, and 807 cells from the LCMV-Clone13 sample.

For human skin samples, scRNAseq datasets were processed with CellRanger v3.1.0 and output data analysis was performed using the Seurat package v4.1.0. All cells identified in the CellRanger expression matrices were filtered to exclude those with fewer than 500 transcripts, low RNA complexity (log10 genes per UMI < 0.8), and greater than 20% mitochondrial transcripts. 19,851, 11,955, and 4,209 cells were included in the dataset for

lesional, non-lesional and healthy skin samples, respectively. Genes expressed in fewer than 5 total cells were excluded from further analysis. Data from multiple samples was integrated using the Seurat IntegrateData workflow. The combined data was scaled and principal component analysis (PCA) was performed. After review of principal component contributions to variance, UMAP was performed using the first 40 PCs. Clustering was performed using shared nearest neighbor clustering in Seurat with a resolution of 0.25 (chosen based on iterative analysis). Cluster identification was based on marker expression as identified by Seurat's FindConservedMarkers and FindAllMarkers functions. Clusters representing cell types of interest were isolated using the Seurat subset function. Subsets were re-scaled, and another iteration of PCA and UMAP was performed, after which sub-clustering was performed using FindClusters with resolution varying by cell type and chosen based on iterative analysis of clustering results. Differential expression analysis was performed using the "RNA" assay, with scatter plot, dot plot, violin plot, and heatmap visualizations constructed using the appropriate Seurat functions and colored / annotated / scaled using the ggplot package.

Other quantifications, statistical analyses and renderings

FlowJo v10.8.1 software was used for flow cytometric analysis. Prism v9.5.0 software was used to determine statistical significance using Student's two-tailed unpaired *t* or Mann Whitney tests. *P* values are indicated in each figure legend. Parts of Figures 1A and 5A and Supplementary Figure 2A were created with BioRender.com under publication license CU258HTCZ9.

Extended Data

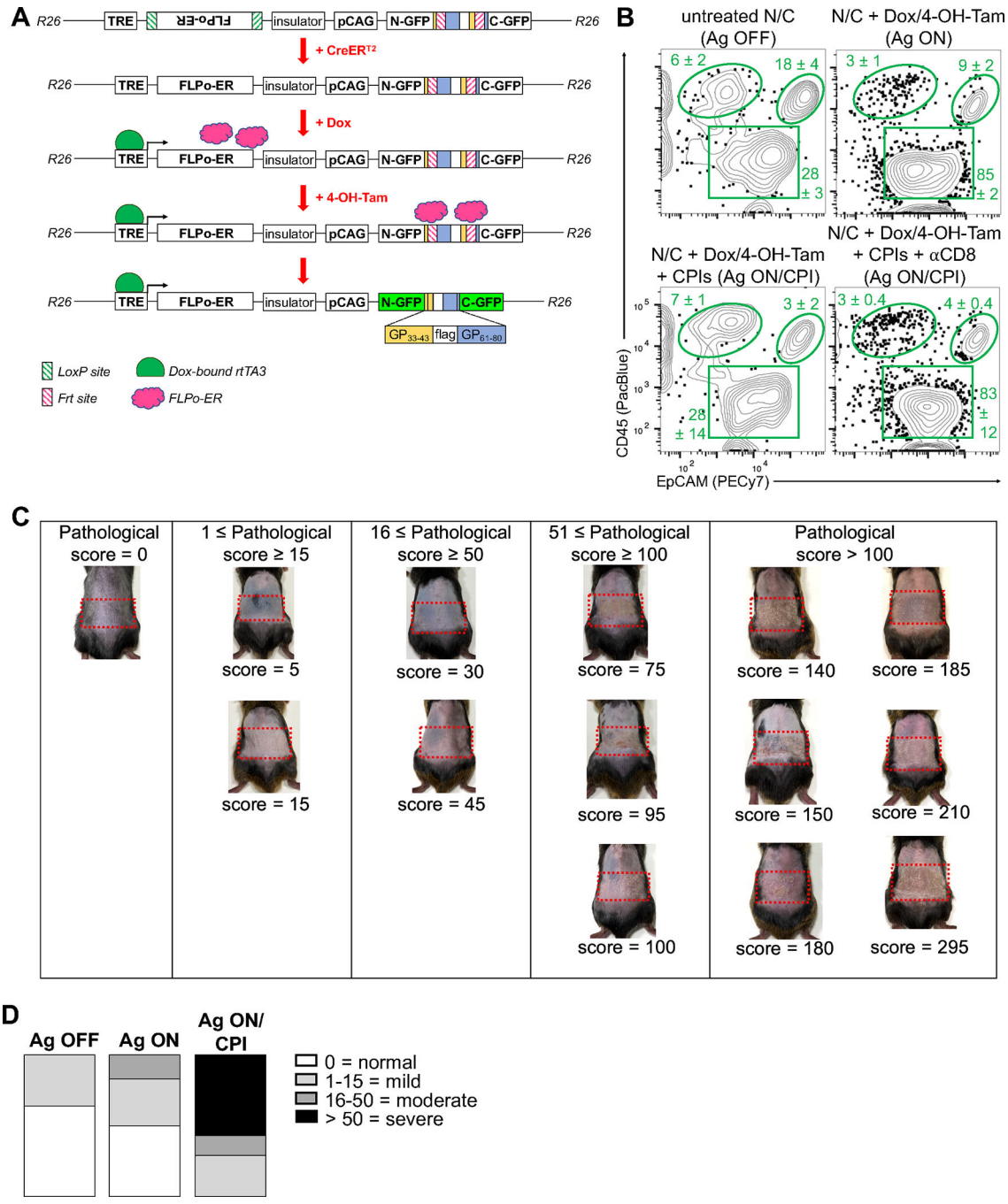

Extended Data Figure 1 - Induction of Ag expression in EpCAM+CD45- skin cells coupled to CPIs leads to quantifiable cutaneous pathology

A) NINJA allele and Dox/4-OH-Tam-driven recombinations required for induction of NINJA Ag expression. B) Average ± s.d. of frequencies of Ag (GFP)-expressing skin cell populations identified by EpCAM and CD45 expression. n = 3 (Ag ON, Ag ON/ CPI, Ag ON/CPI + αCD8) or 6 (Ag OFF), representative of > 3 experimental repeats. C) Representative pictures of cutaneous pathology by range of pathological scores. D)

Frequency of pathological scores by experimental condition. n = 6 (Ag ON) or 7 (Ag OFF, Ag ON/CPI), representative of > 3 experimental repeats.

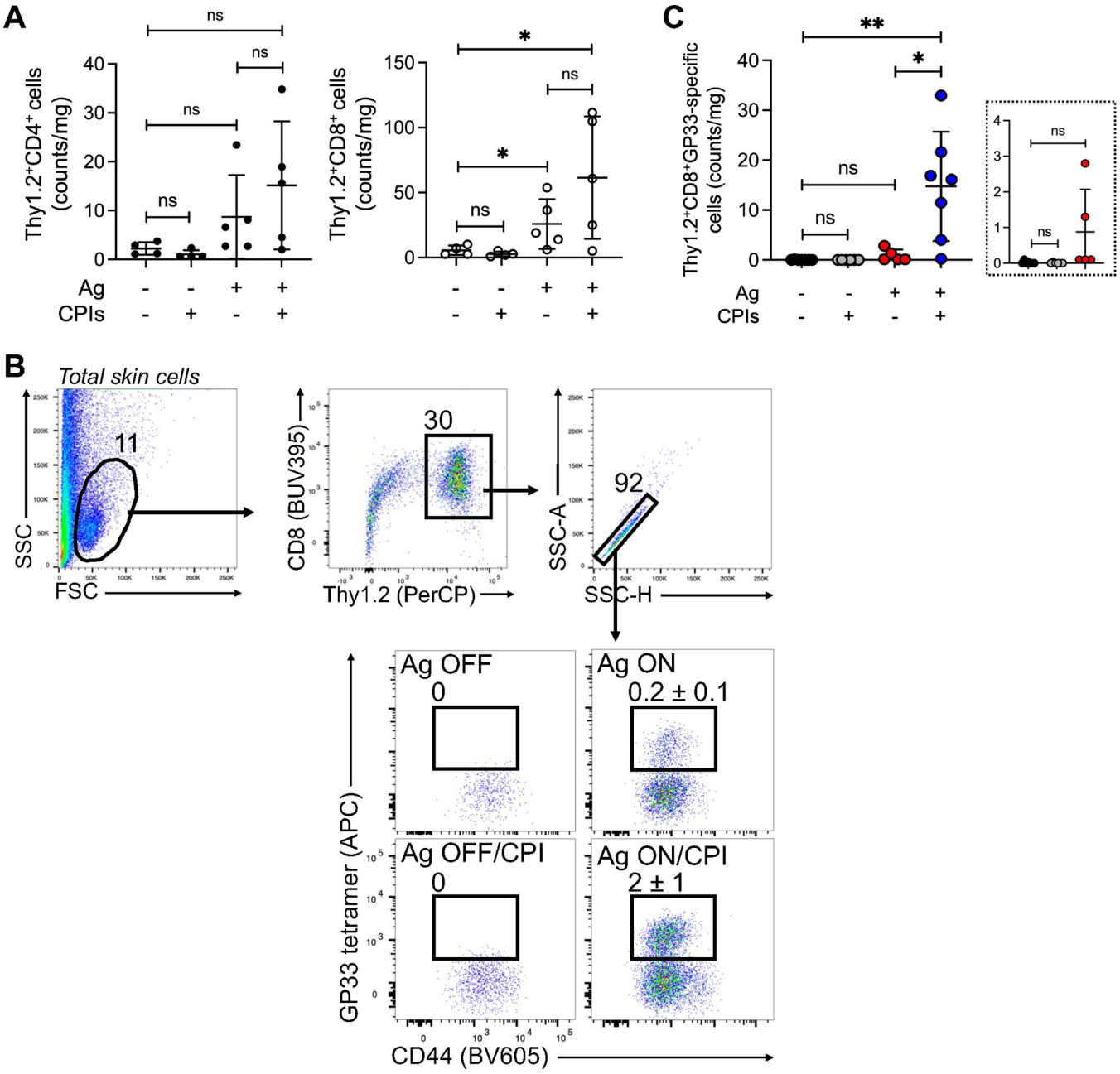

Extended Data Figure 2 - Ag-specific CD8 T cells infiltrate skin upon local Ag expression with and without CPIs

A) Average ± s.d. of normalized counts of skin-infiltrating CD4 and CD8 T cells from mice in the indicated conditions. * $P = 0.0495$ (Ag ON vs. Ag OFF), * $P = 0.0437$ (Ag ON/CPI vs. Ag OFF), and ns = not significant by two-tailed t test. n = 4 (Ag OFF, Ag OFF/CPI) or 5 (Ag ON, Ag ON/CPI), representative of 3 experimental repeats. B) Gating strategy and average ± s.d. of frequencies of gated populations from skin in the indicated experimental

conditions. n = 5 (Ag OFF, Ag OFF/CPI) or 6 (Ag ON, Ag ON/CPI), representative of 3 experimental repeats. C) Average ± s.d. of normalized counts of endogenous GP33-specific CD8 T cells from skin of mice in the indicated experimental conditions. * $P = 0.0196$, ** $P = 0.004$ and ns = not significant by two-tailed t test. n = 5 (Ag ON); 6 (Ag OFF/CPI); or 7 (Ag OFF, Ag ON/CPI). Representative of 3 experimental repeats.

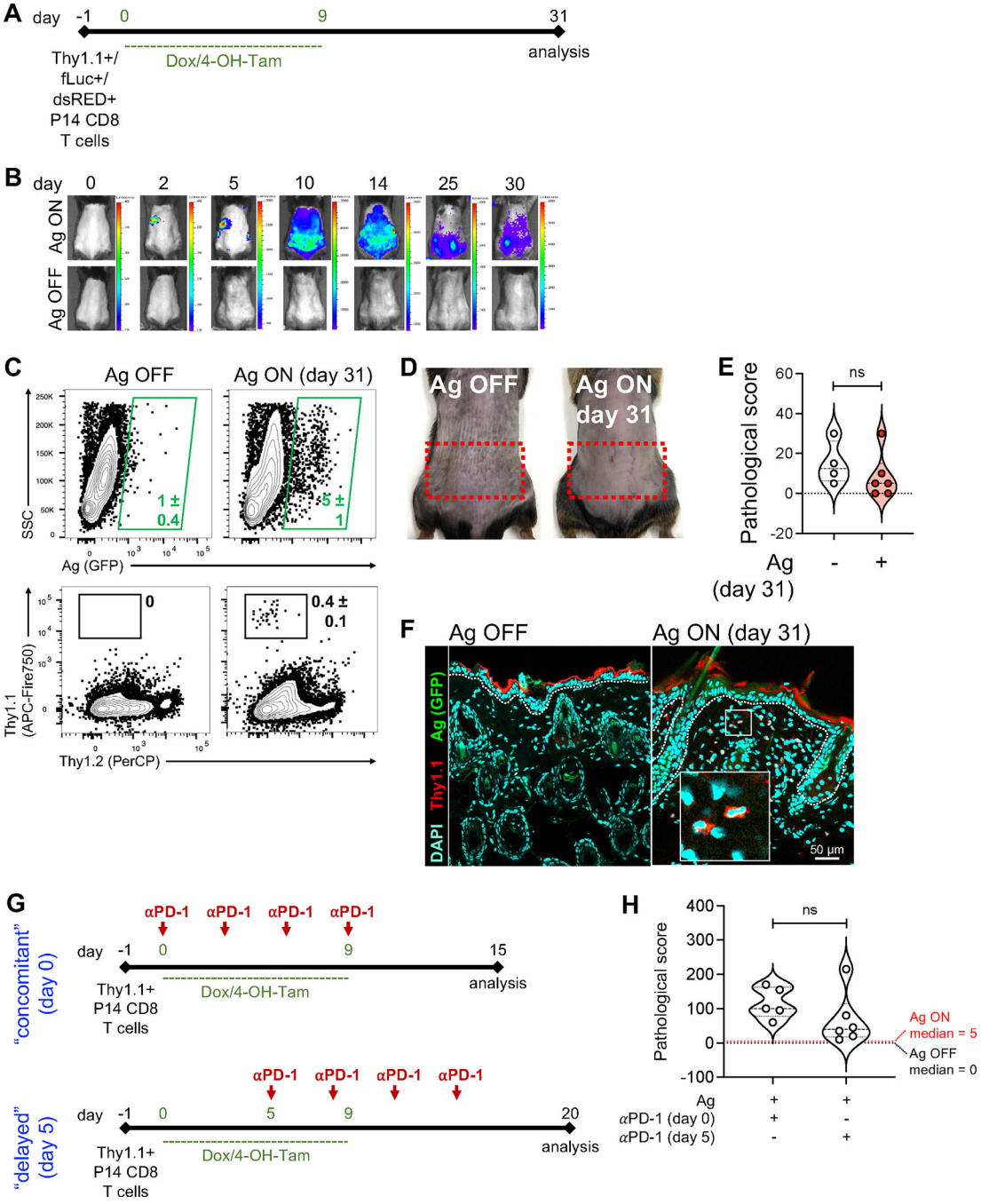

Extended Data Figure 3 - PD-1 allows Ag-specific CD8 T cells to co-exist with Ag-expressing skin cells without local pathology

A) Experimental schedule. B) IVIS imaging of fLuc-expressing P14 CD8 T cells in representative mice from the indicated conditions. n = 4 (Ag OFF) or 6 (Ag ON), representative of 2 experimental repeats. C) Average ± s.d. of frequencies of Ag (GFP)-expressing skin cells (top) and Thy1.1+ P14 CD8 T cells (bottom) in 4-OH-Tam-treated skin from mice in the indicated conditions. n = 4 (Ag OFF) or 6 (Ag ON), representative of 2 experimental repeats. D) Representative pictures of the back of mice from the indicated conditions in C. E) Pathological scores assigned to mice in the indicated conditions in C. ns = not significant by two-tailed *t* test. F) Confocal microscopy analysis of skin from mice in C. Dotted line = epidermis (top)/dermis (bottom) interface. G) Experimental schedule for comparison of concomitant vs. delayed administration of αPD-1 antibodies in Dox/4-OH-Tam-treated N/C mice. H) Pathological scores of mice from the indicated conditions. Black and red dotted lines indicate median pathological scores of Ag OFF and Ag ON conditions, respectively, from Fig 1E. ns = not significant by two-tailed *t* test. n = 5 (day 0) or 6 (day 5), representative of 2 experimental repeats.

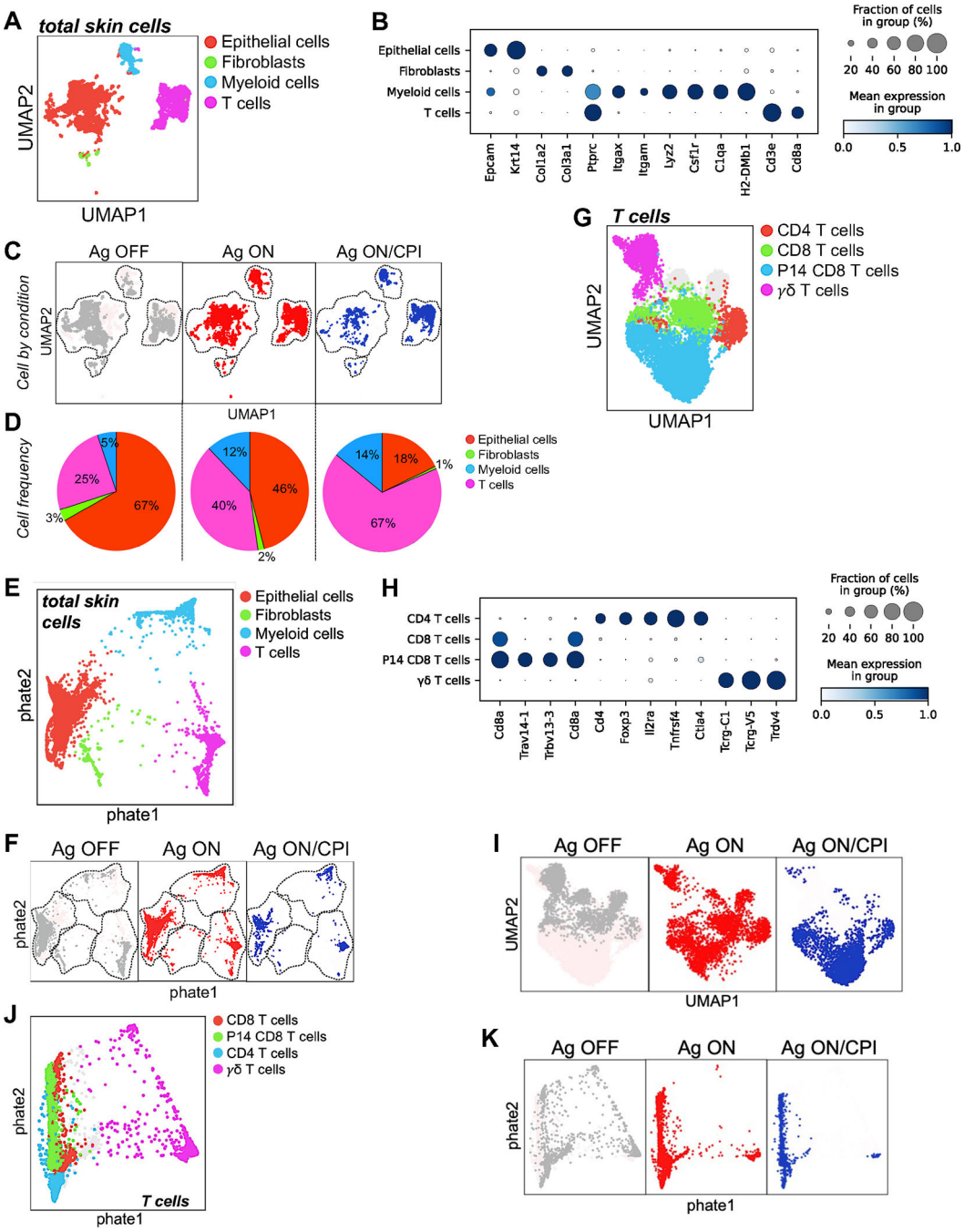

Extended Data Figure 4 - Skin-specific Ag expression leads to changes in local cell populations identified by scRNAseq analysis

A) UMAP projection of total skin cells sequenced across experimental samples and annotated by cell type. n = 21,178 total cells sequenced. B) Dot plot of genes defining populations of skin cells shown in A. C) UMAP projections of total skin cells from A by experimental condition. D) Frequencies of skin cell types from A by experimental condition. E) PHATE map of total skin cells sequenced across experimental samples and annotated by cell type. F) PHATE maps of total skin cells from E by experimental condition. G) UMAP projection of *Cd3e*-expressing cells from A sequenced across experimental samples

and annotated by T cell type. H) Dot plot of genes defining populations of *CD3e*-expressing cells in skin in G. I) UMAP projections of *Cd3e*-expressing cells in G by experimental condition. J) PHATE map of *Cd3e*-expressing cells from E annotated by T cell type. K) PHATE maps of *Cd3e*-expressing cells in J by experimental condition.

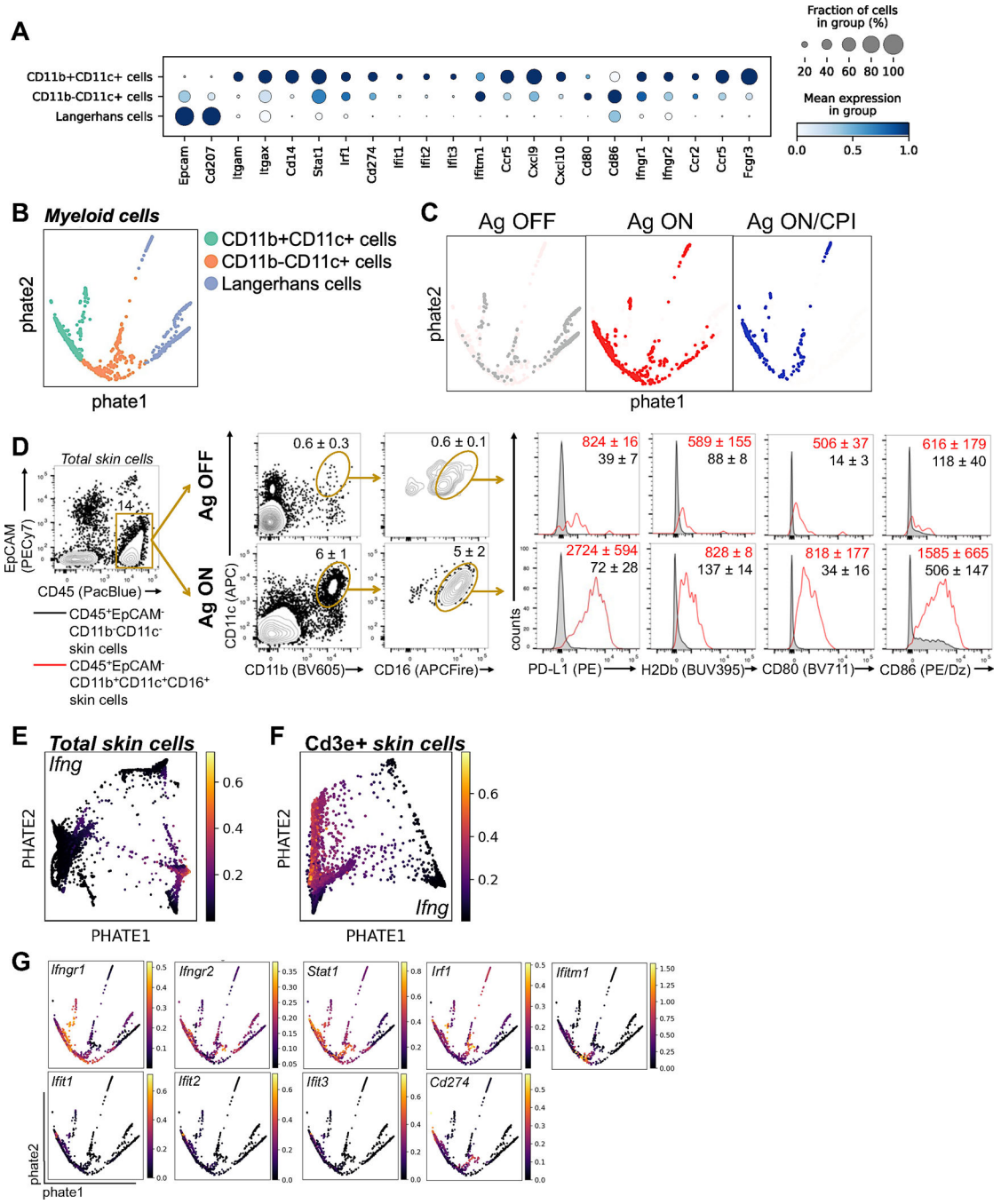

Extended Data Figure 5 - Transcriptomic analysis of myeloid cell populations from the skin of Ag OFF, Ag ON and Ag ON/CPI mice

A) Dot plot of genes defining populations of skin-infiltrating myeloid cells from Figure 4A. B) PHATE map of myeloid cell populations sequenced across experimental samples.

C) PHATE maps of myeloid cell populations in B by experimental condition. D) Gating strategy and representative histograms for skin-infiltrating CD11b+CD11c+CD16+ cells in the indicated conditions. Numbers represent average ± s.d. of frequencies of the gated populations (dot plots) or average ± s.d. of MFIs of the indicated markers (histograms). n = 3, representative of 3 experimental repeats. E) PHATE map of *Ifng* expression by total skin cells from Extended Data Figure 4E. F) PHATE map of *Ifng* expression by *CD3e*+ skin cells from Extended Data Figure 4J. G) PHATE maps of expression level of the indicated genes by skin-infiltrating myeloid cells sequenced across samples shown in B.

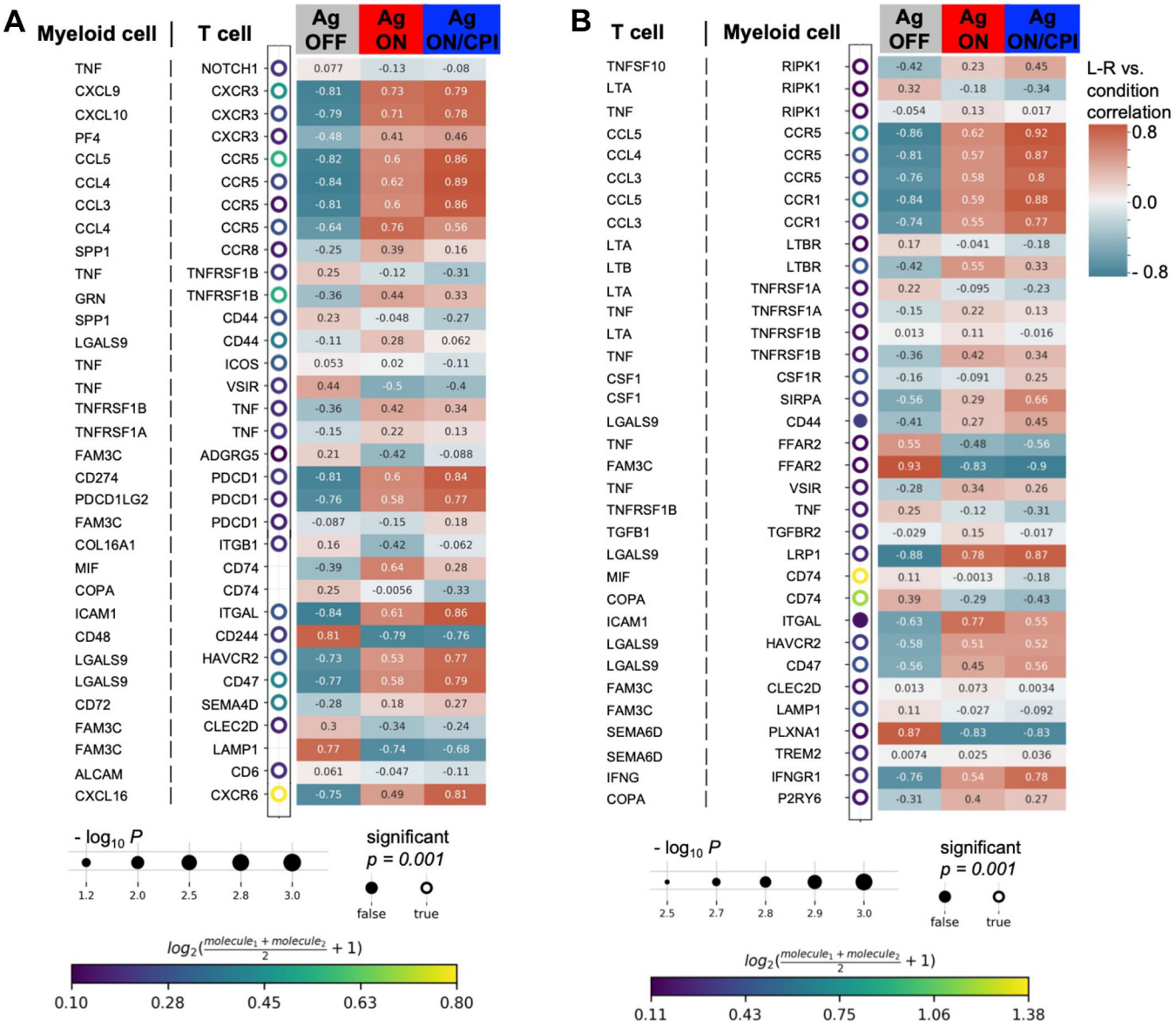

Extended Data Figure 6 - Multi-layer interactions between skin-infiltrating myeloid cells and T cells are revealed by scRNAseq analysis

A,B) CellPhoneDB algorithm and Pearson correlation analysis of the gene expression levels of the indicated ligand/receptor pairs in skin-infiltrating myeloid cells and T cells (A) and T

cells and myeloid cells (B), respectively, sequenced from mice in the indicated experimental conditions. One-sided *P* values are shown.

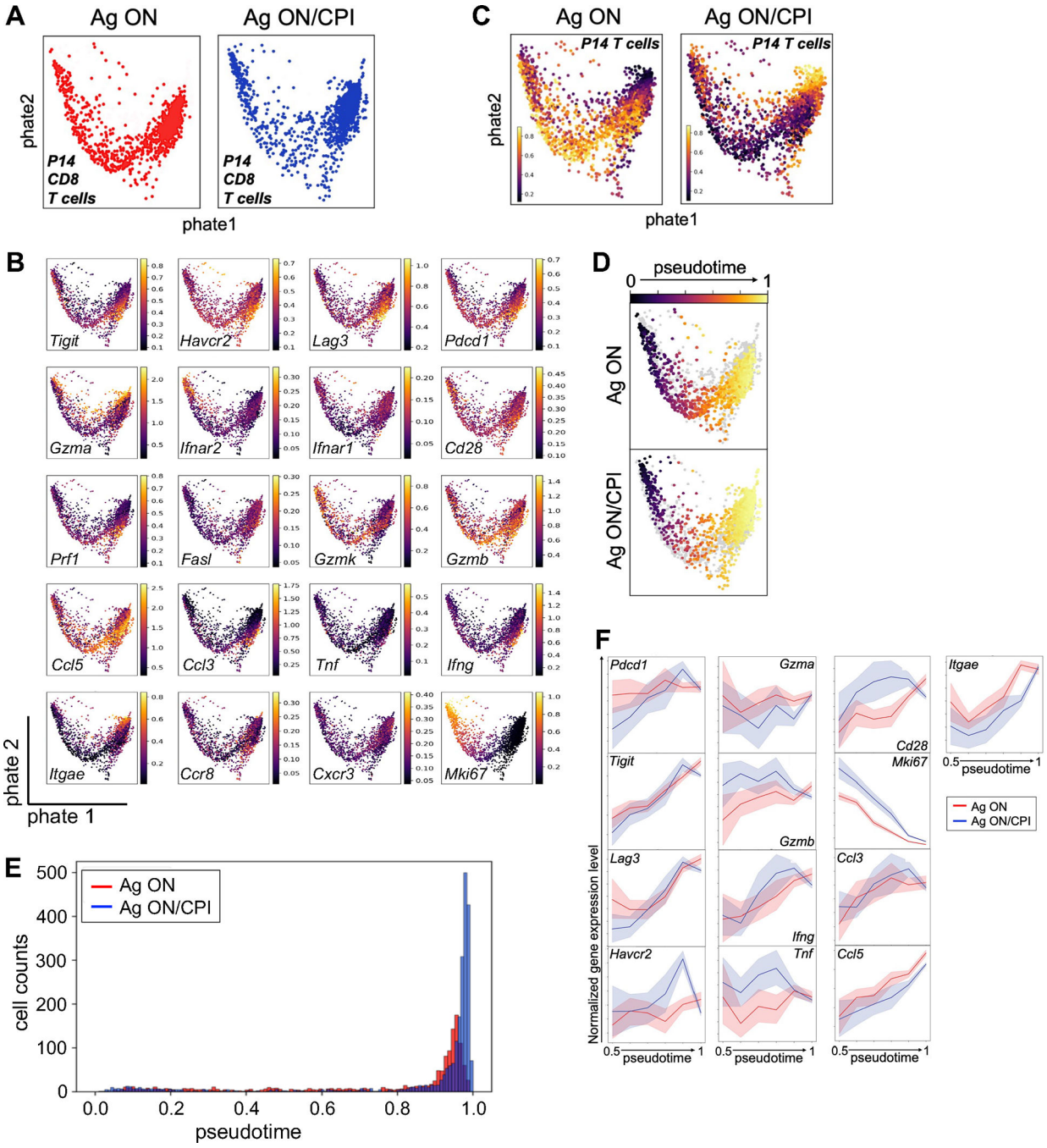

Extended Data Figure 7 - Transcriptomic analysis of P14 CD8 T cells from the skin of Ag ON and Ag ON/CPI mice

A) PHATE maps of skin-infiltrating P14 CD8 T cells sequenced in the indicated experimental conditions. B) PHATE maps of expression level of the indicated genes by skin-infiltrating P14 CD8 T cells sequenced across samples. C) PHATE maps of the likelihood of skin-infiltrating P14 CD8 T cells calculated by MELD. D) PHATE maps

of the pseudotime analysis of skin-infiltrating P14 CD8 T cells sequenced across samples. E) Skin-infiltrating P14 CD8 T cell number distribution along the pseudotime shown by experimental condition. F) Z-score-normalized expression levels of the indicated genes over pseudotime in skin-infiltrating P14 CD8 T cells in B.

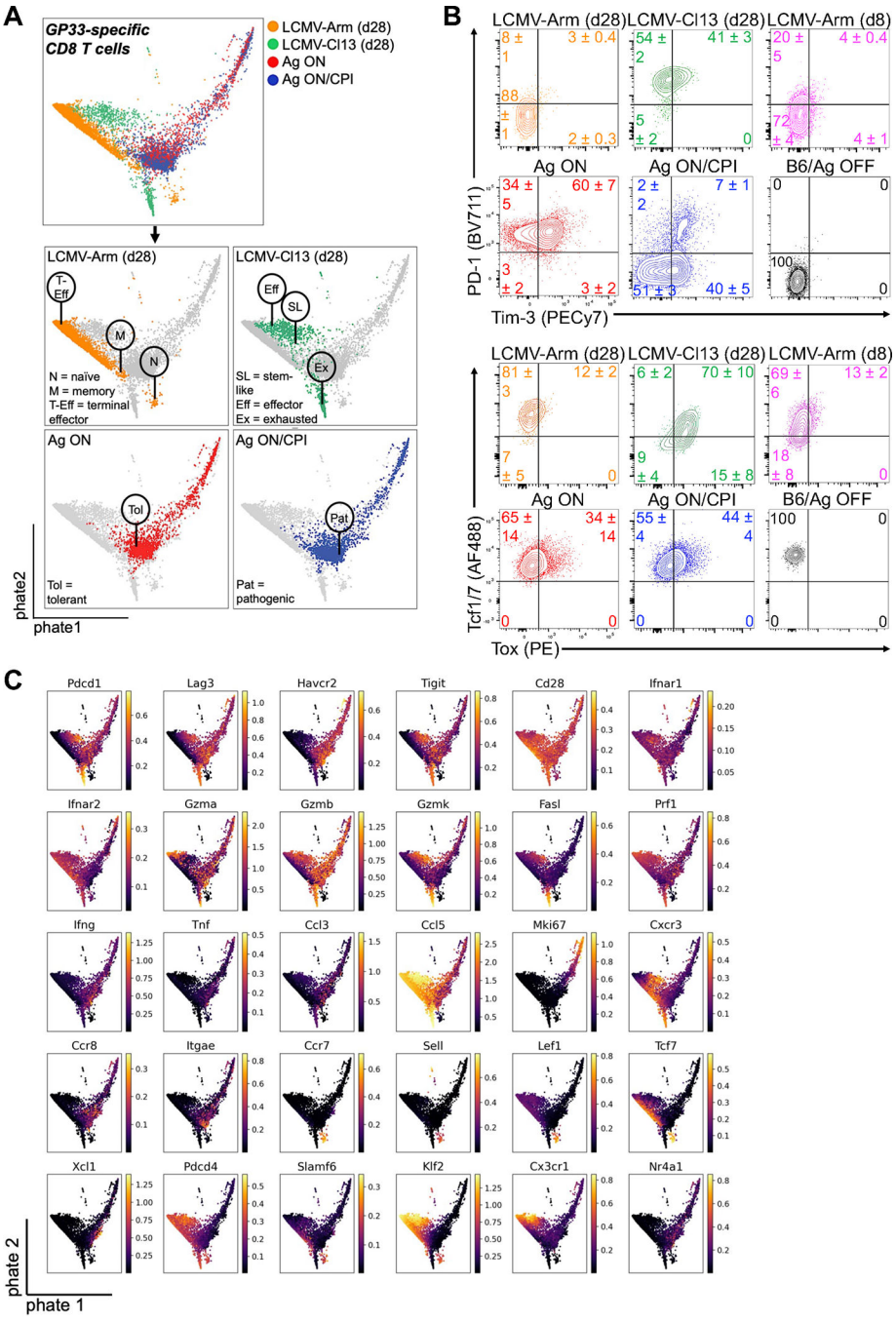

Extended Data Figure 8 - Integrated transcriptomic analysis supports a linear differentiation trajectory for skin Ag-specific CD8 T cells

A) PHATE map of skin-infiltrating P14 CD8 T cells from Ag ON and Ag ON/CPI mice and GP33-specific CD8 T cells from an LCMV-Clone13-infected B6 mouse (28 days

post infection) and GP33-specific CD8 T cells from an LCMV-Armstrong-infected B6 mouse (28 days post infection). B) Average ± s.d. of frequencies of gated populations of skin-infiltrating P14 CD8 T cells from Ag ON and Ag ON/CPI mice, and GP33-specific CD8 T cells from the spleen of LCMV-Clone13-infected B6 mice (28 days post infection) or LCMV-Armstrong-infected B6 mice (8 or 28 days post infection). Naïve CD44^{-} CD8 T cells from the spleen of one B6 mouse are shown as negative controls. n = 3 (LCMV-infected mice); 4 (Ag ON); or 5 (Ag ON/CPI). Representative of 2 experimental repeats. C) PHATE maps of expression level of the indicated genes by skin-infiltrating P14 CD8 T cells and GP33-specific CD8 T cells in A.

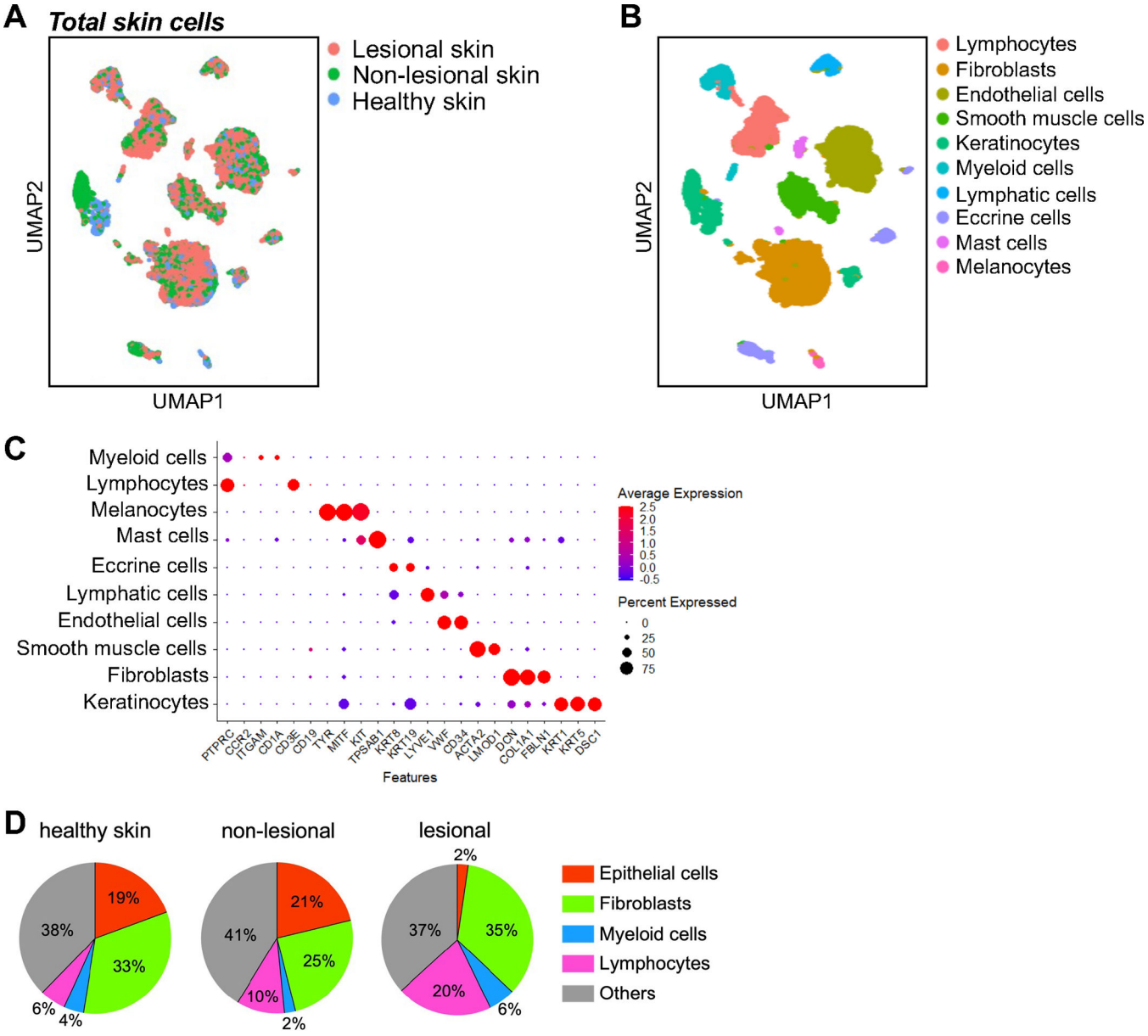

Extended Data Figure 9 - Transcriptomic analysis by scRNAseq of human skin from healthy donors and patients with cutaneous lichenoid irAEs

A) UMAP projection of scRNAseq data from total cells harvested from matched lesional and non-lesional skin of two patients with lichenoid irAEs and from three healthy donors. n = 19,851, 11,955, and 4,209 cells from lesional, non-lesional and healthy skin samples, respectively. B) UMAP projection of the dataset in A color-coded by cell population. C) Dot plot of genes defining the cell populations identified in B. D) Frequencies of the skin cell populations in B.

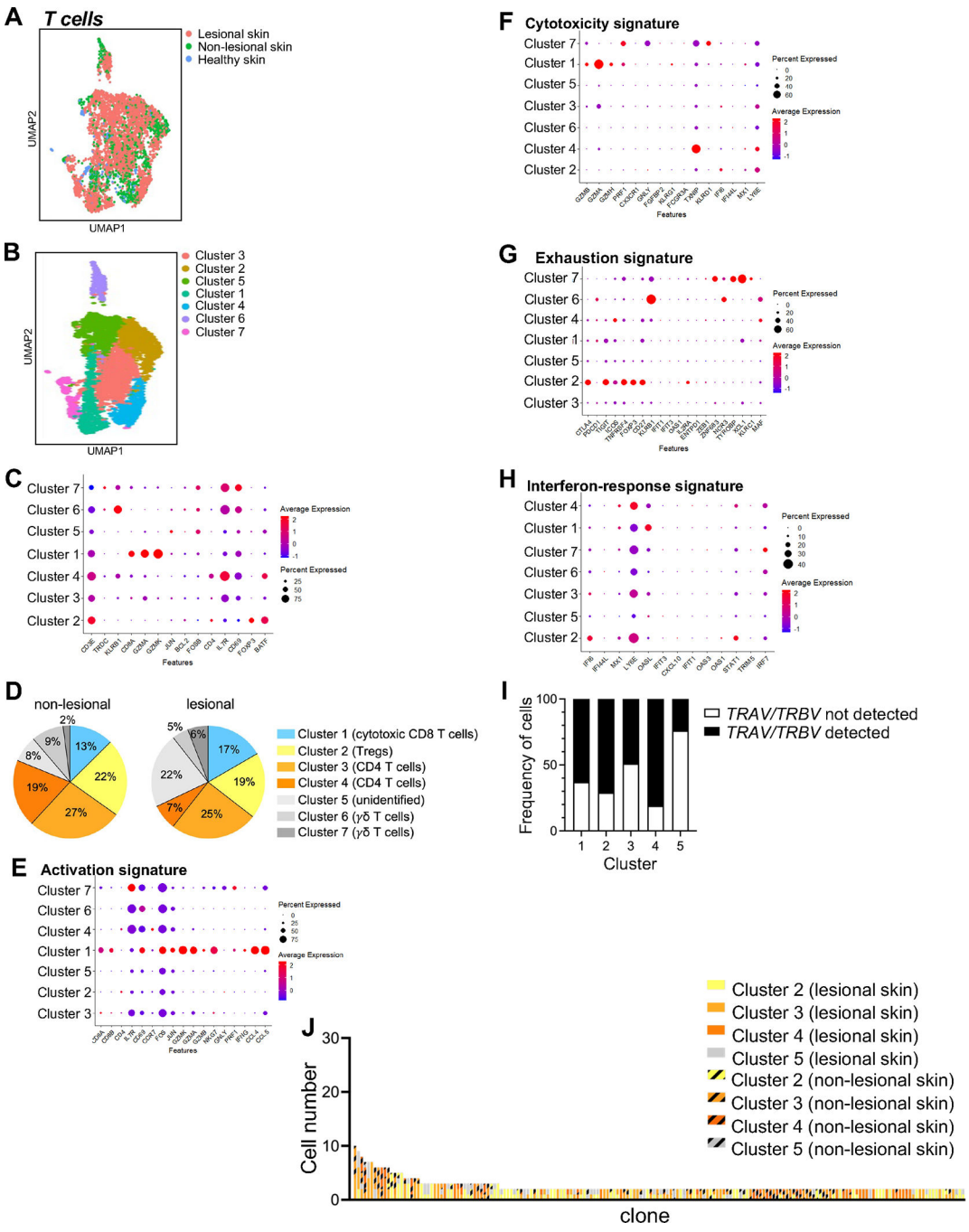

Extended Data Figure 10 - CD8 T cells with a cytotoxic gene expression profile infiltrate healthy and diseased skin in patients with cutaneous lichenoid irAEs

A) UMAP projection of *CD3e*-expressing skin cells from the dataset shown in Extended Data Figure 9. B) UMAP projection of *CD3e*-expressing skin cells in A color-coded by Cluster. C) Dot plot of genes defining individual Clusters in B. D) Frequencies of the T cell populations identified in B in lesional vs. non-lesional skin. E-H) Dot plot of genes characterizing activation, cytotoxicity, exhaustion and interferon-response signatures[48] in T cell Clusters from B,C. I) Frequency of cells with and without associated *TRAV/TRBV* sequences from Clusters 1–5 defined in B,C. J) Number and size of all T cell clones from Clusters 2–5 sequenced in lesional and non-lesional skin.

Supplementary Material

Refer to Web version on PubMed Central for supplementary material.

Acknowledgements

We thank Joshi lab members for helpful discussions and reviewing the manuscript. We are thankful to M. Huelsmeyer for tool supply. We also thank the Yale Flow Cytometry Core, Yale School of Medicine Comparative Pathology Research Core, and the Yale Center for Genome Analysis. The Yale Flow Cytometry Core is supported in part by NIH grant P30CA016359 and S10OD026996. This work was supported by grants from The G. Harold & Leila Y. Mathers Foundation (YAL182 to N.S.J.), the Melanoma Research Alliance (569588 to N.S.J.), the Yale SPORE in Skin Cancer (2P50CA196530–06 to N.S.J.), the Yale Liver Center Morphology Core (NIH grant P30DK034989), and the American Cancer Society (Research Scholar Award to N.S.J). M.D. was supported by the Leslie H. Warner Post-Doctoral Research Fellowship. N.I.H. was supported by the Dermatology Foundation.

Data availability

The scRNAseq datasets from Ag OFF, Ag ON and Ag ON/CPI mice are available from the GEO database under accession number GSE228586.

The scRNAseq datasets from LCMV-Armstrong- and LCMV-Clone13-infected mice are available from the GEO database under accession numbers GSE182509 and GSM5530565.

The scRNAseq datasets from human donors are available from the GEO database under accession number GSE229279.

References

1. Maeda Y et al. Detection of self-reactive $CD8^+$ T cells with an anergic phenotype in healthy individuals. Science 346, 1536–1540, doi:10.1126/science.aaa1292 (2014). [PubMed: 25525252]
2. Yu W et al. Clonal Deletion Prunes but Does Not Eliminate Self-Specific αβ CD8(+) T Lymphocytes. Immunity 42, 929–941, doi:10.1016/j.immuni.2015.05.001 (2015). [PubMed: 25992863]
3. ElTanbouly MA & Noelle RJ Rethinking peripheral T cell tolerance: checkpoints across a T cell's journey. Nat Rev Immunol 21, 257–267, doi:10.1038/s41577-020-00454-2 (2021). [PubMed: 33077935]
4. Redmond WL & Sherman LA Peripheral tolerance of CD8 T lymphocytes. Immunity 22, 275–284, doi:10.1016/j.immuni.2005.01.010 (2005). [PubMed: 15780985]
5. Probst HC, Lagnel J, Kollias G & van den Broek M Inducible transgenic mice reveal resting dendritic cells as potent inducers of CD8+ T cell tolerance. Immunity 18, 713–720, doi:10.1016/s1074-7613(03)00120-1 (2003). [PubMed: 12753747]
6. Parish IA et al. The molecular signature of CD8+ T cells undergoing deletional tolerance. Blood 113, 4575–4585, doi:10.1182/blood-2008-10-185223 (2009). [PubMed: 19204323]

7. Nishimura H, Nose M, Hiai H, Minato N & Honjo T Development of lupus-like autoimmune diseases by disruption of the PD-1 gene encoding an ITIM motif-carrying immunoreceptor. Immunity 11, 141–151, doi:10.1016/s1074-7613(00)80089-8 (1999). [PubMed: 10485649]
8. Liang SC et al. Regulation of PD-1, PD-L1, and PD-L2 expression during normal and autoimmune responses. Eur J Immunol 33, 2706–2716, doi:10.1002/eji.200324228 (2003). [PubMed: 14515254]
9. Probst HC, McCoy K, Okazaki T, Honjo T & van den Broek M Resting dendritic cells induce peripheral CD8+ T cell tolerance through PD-1 and CTLA-4. Nat Immunol 6, 280–286, doi:10.1038/ni1165 (2005). [PubMed: 15685176]
10. Keir ME et al. Tissue expression of PD-L1 mediates peripheral T cell tolerance. J Exp Med 203, 883–895, doi:10.1084/jem.20051776 (2006). [PubMed: 16606670]
11. Martin-Orozco N, Wang YH, Yagita H & Dong C Cutting Edge: Programmed death (PD) ligand-1/PD-1 interaction is required for CD8+ T cell tolerance to tissue antigens. J Immunol 177, 8291–8295, doi:10.4049/jimmunol.177.12.8291 (2006). [PubMed: 17142723]
12. Keir ME, Freeman GJ & Sharpe AH PD-1 regulates self-reactive CD8+ T cell responses to antigen in lymph nodes and tissues. J Immunol 179, 5064–5070, doi:10.4049/jimmunol.179.8.5064 (2007). [PubMed: 17911591]
13. Pauken KE et al. Cutting edge: identification of autoreactive CD4+ and CD8+ T cell subsets resistant to PD-1 pathway blockade. J Immunol 194, 3551–3555, doi:10.4049/jimmunol.1402262 (2015). [PubMed: 25769925]
14. Nelson CE et al. Reprogramming responsiveness to checkpoint blockade in dysfunctional CD8 T cells. Proc Natl Acad Sci U S A 116, 2640–2645, doi:10.1073/pnas.1810326116 (2019). [PubMed: 30679280]
15. Postow MA, Sidlow R & Hellmann MD Immune-Related Adverse Events Associated with Immune Checkpoint Blockade. N Engl J Med 378, 158–168, doi:10.1056/NEJMra1703481 (2018). [PubMed: 29320654]
16. Johnson DB et al. Fulminant Myocarditis with Combination Immune Checkpoint Blockade. N Engl J Med 375, 1749–1755, doi:10.1056/NEJMoa1609214 (2016). [PubMed: 27806233]
17. Shi VJ et al. Clinical and Histologic Features of Lichenoid Mucocutaneous Eruptions Due to Anti-Programmed Cell Death 1 and Anti-Programmed Cell Death Ligand 1 Immunotherapy. JAMA Dermatol 152, 1128–1136, doi:10.1001/jamadermatol.2016.2226 (2016). [PubMed: 27411054]
18. Luoma AM et al. Molecular Pathways of Colon Inflammation Induced by Cancer Immunotherapy. Cell 182, 655–671.e622, doi:10.1016/j.cell.2020.06.001 (2020). [PubMed: 32603654]
19. Yasuda Y et al. CD4(+) T cells are essential for the development of destructive thyroiditis induced by anti-PD-1 antibody in thyroglobulin-immunized mice. Sci Transl Med 13, doi:10.1126/scitranslmed.abb7495 (2021).
20. Reschke R et al. Checkpoint Blockade-Induced Dermatitis and Colitis Are Dominated by Tissue-Resident Memory T Cells and Th1/Tc1 Cytokines. Cancer Immunol Res 10, 1167–1174, doi:10.1158/2326-6066.Cir-22-0362 (2022). [PubMed: 35977003]
21. Khan S & Gerber DE Autoimmunity, checkpoint inhibitor therapy and immune-related adverse events: A review. Semin Cancer Biol 64, 93–101, doi:10.1016/j.semcancer.2019.06.012 (2020). [PubMed: 31330185]
22. Medetgul-Ernar K & Davis MM Standing on the shoulders of mice. Immunity 55, 1343–1353, doi:10.1016/j.immuni.2022.07.008 (2022). [PubMed: 35947979]
23. Damo M et al. Inducible de novo expression of neoantigens in tumor cells and mice. Nat Biotechnol 39, 64–73, doi:10.1038/s41587-020-0613-1 (2021). [PubMed: 32719479]
24. Ventura A et al. Restoration of p53 function leads to tumour regression in vivo. Nature 445, 661–665, doi:10.1038/nature05541 (2007). [PubMed: 17251932]
25. Kaur H, Nikam BP, Jamale VP & Kale MS Lichen Planus Severity Index: A new, valid scoring system to assess the severity of cutaneous lichen planus. Indian J Dermatol Venereol Leprol 86, 169–175, doi:10.4103/ijdvl.IJDVL_650_17 (2020). [PubMed: 31898636]
26. Pircher H, Bürki K, Lang R, Hengartner H & Zinkernagel RM Tolerance induction in double specific T-cell receptor transgenic mice varies with antigen. Nature 342, 559–561, doi:10.1038/342559a0 (1989). [PubMed: 2573841]

27. Moon KR et al. Visualizing structure and transitions in high-dimensional biological data. Nat Biotechnol 37, 1482–1492, doi:10.1038/s41587-019-0336-3 (2019). [PubMed: 31796933]
28. Garcia-Diaz A et al. Interferon Receptor Signaling Pathways Regulating PD-L1 and PD-L2 Expression. Cell Rep 19, 1189–1201, doi:10.1016/j.celrep.2017.04.031 (2017). [PubMed: 28494868]
29. Efremova M, Vento-Tormo M, Teichmann SA & Vento-Tormo R CellPhoneDB: inferring cell-cell communication from combined expression of multi-subunit ligand-receptor complexes. Nat Protoc 15, 1484–1506, doi:10.1038/s41596-020-0292-x (2020). [PubMed: 32103204]
30. Hofmann M & Pircher H E-cadherin promotes accumulation of a unique memory CD8 T-cell population in murine salivary glands. Proc Natl Acad Sci U S A 108, 16741–16746, doi:10.1073/pnas.1107200108 (2011). [PubMed: 21930933]
31. Burkhardt DB et al. Quantifying the effect of experimental perturbations at single-cell resolution. Nat Biotechnol 39, 619–629, doi:10.1038/s41587-020-00803-5 (2021). [PubMed: 33558698]
32. Hudson WH et al. Proliferating Transitory T Cells with an Effector-like Transcriptional Signature Emerge from PD-1(+) Stem-like CD8(+) T Cells during Chronic Infection. Immunity 51, 1043–1058.e1044, doi:10.1016/j.immuni.2019.11.002 (2019). [PubMed: 31810882]
33. Kaech SM, Hemby S, Kersh E & Ahmed R Molecular and functional profiling of memory CD8 T cell differentiation. Cell 111, 837–851, doi:10.1016/s0092-8674(02)01139-x (2002). [PubMed: 12526810]
34. Schaberg KB et al. Immunohistochemical analysis of lichenoid reactions in patients treated with anti-PD-L1 and anti-PD-1 therapy. J Cutan Pathol 43, 339–346, doi:10.1111/cup.12666 (2016). [PubMed: 26762844]
35. Zehn D & Bevan MJ T cells with low avidity for a tissue-restricted antigen routinely evade central and peripheral tolerance and cause autoimmunity. Immunity 25, 261–270, doi:10.1016/j.immuni.2006.06.009 (2006). [PubMed: 16879996]
36. Marchingo JM & Cantrell DA Protein synthesis, degradation, and energy metabolism in T cell immunity. Cell Mol Immunol 19, 303–315, doi:10.1038/s41423-021-00792-8 (2022). [PubMed: 34983947]
37. Zinselmeyer BH et al. PD-1 promotes immune exhaustion by inducing antiviral T cell motility paralysis. J Exp Med 210, 757–774, doi:10.1084/jem.20121416 (2013). [PubMed: 23530125]
38. Fife BT et al. Interactions between PD-1 and PD-L1 promote tolerance by blocking the TCR-induced stop signal. Nat Immunol 10, 1185–1192, doi:10.1038/ni.1790 (2009). [PubMed: 19783989]
39. Vella JL et al. Dendritic cells maintain anti-tumor immunity by positioning CD8 skin-resident memory T cells. Life Sci Alliance 4, doi:10.26508/lsa.202101056 (2021).
40. Miller BC et al. Subsets of exhausted CD8(+) T cells differentially mediate tumor control and respond to checkpoint blockade. Nat Immunol 20, 326–336, doi:10.1038/s41590-019-0312-6 (2019). [PubMed: 30778252]
41. Im SJ et al. Defining CD8+ T cells that provide the proliferative burst after PD-1 therapy. Nature 537, 417–421, doi:10.1038/nature19330 (2016). [PubMed: 27501248]
42. Yost KE et al. Clonal replacement of tumor-specific T cells following PD-1 blockade. Nat Med 25, 1251–1259, doi:10.1038/s41591-019-0522-3 (2019). [PubMed: 31359002]
43. Dammeijer F et al. The PD-1/PD-L1-Checkpoint Restrains T cell Immunity in Tumor-Draining Lymph Nodes. Cancer Cell 38, 685–700.e688, doi:10.1016/j.ccell.2020.09.001 (2020). [PubMed: 33007259]
44. Francis DM et al. Blockade of immune checkpoints in lymph nodes through locoregional delivery augments cancer immunotherapy. Sci Transl Med 12, doi:10.1126/scitranslmed.aay3575 (2020).
45. Im SJ, Konieczny BT, Hudson WH, Masopust D & Ahmed R PD-1+ stemlike CD8 T cells are resident in lymphoid tissues during persistent LCMV infection. Proc Natl Acad Sci U S A 117, 4292–4299, doi:10.1073/pnas.1917298117 (2020). [PubMed: 32034098]
46. Nüssing S et al. Efficient CRISPR/Cas9 Gene Editing in Uncultured Naive Mouse T Cells for In Vivo Studies. J Immunol 204, 2308–2315, doi:10.4049/jimmunol.1901396 (2020). [PubMed: 32152070]

47. van Dijk D et al. Recovering Gene Interactions from Single-Cell Data Using Data Diffusion. Cell 174, 716–729.e727, doi:10.1016/j.cell.2018.05.061 (2018). [PubMed: 29961576]

48. Dunlap GS et al. Single-cell transcriptomics reveals distinct effector profiles of infiltrating T cells in lupus skin and kidney. JCI Insight 7, doi:10.1172/jci.insight.156341 (2022).

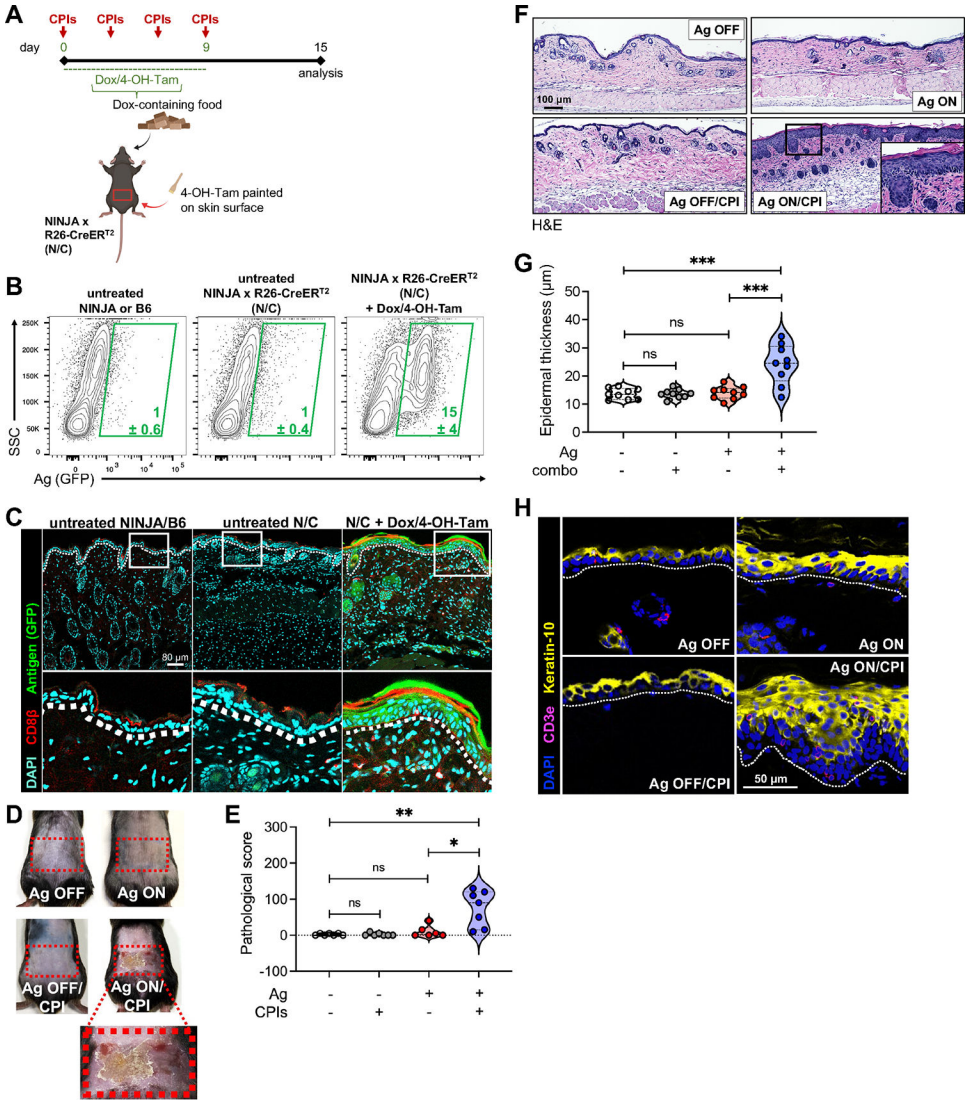

Figure 1 - Skin-specific Ag induction and CPIs lead to local cutaneous disease

A) Experimental schedule. B) Average ± s.d. of frequencies of Ag (GFP)+ skin cells from the indicated conditions. n = 5 (untreated NINJA or B6, N/C) or 7 (N/C + Dox/4-OH-Tam), representative of 4 experimental repeats. C) Confocal microscopy of skin from the indicated conditions. Dotted line = epidermis (top)/dermis (bottom) interface. n = 3, representative of 2 experimental repeats. D) Representative pictures of the back of experimental mice treated as indicated. Red box indicates the 4-OH-Tam-treated area that expresses the NINJA Ags. n = 6 (Ag ON) or 7 (Ag OFF, Ag OFF/CPI, Ag ON/CPI), representative of 3 experimental repeats. E) Pathological scores by experimental condition. * $P = 0.0112$, ** $P = 0.0023$, and ns = not significant by two-tailed t test. n = 6 (Ag ON) or 7 (Ag OFF, Ag OFF/CPI, Ag ON/CPI), representative of 3 experimental repeats. F) H&E staining of skin sections from the indicated conditions. n = 6 (Ag ON) or 7 (Ag OFF, Ag OFF/CPI, Ag ON/CPI), representative of 3 experimental repeats. G) Epidermal thickness quantification by experimental condition. *** $P = 0.0006$ (Ag ON/CPI vs. Ag OFF), *** $P = 0.0008$ (Ag ON/CPI vs. Ag ON), and ns = not significant by two-tailed t test. n = 3 ROIs/mouse for

3 mice, representative of 3 experimental repeats. H) Confocal microscopy of skin from the indicated conditions. Dotted line = epidermis (top)/dermis (bottom) interface. n = 5.

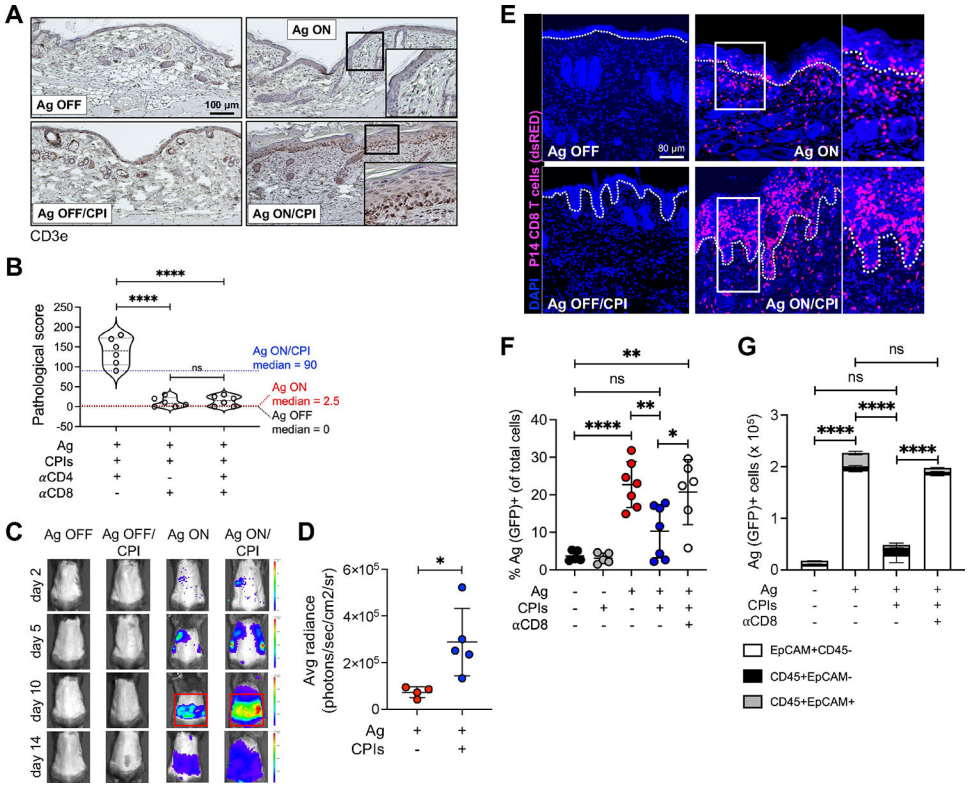

Figure 2 - Ag-specific CD8 T cells cause cutaneous disease by eliminating epidermal Ag-expressing cells

A) CD3e IHC staining of skin sections from the indicated conditions. n = 6, representative of 3 experimental repeats. B) Pathological scores by experimental condition. Black, red and blue dotted lines indicate median pathological scores for T cell-sufficient Ag OFF, Ag ON, and Ag ON/CPI mice, respectively, from Fig 1E. **** $P < 0.0001$ and ns = not significant by two-tailed *t* test. n = 6, pool of 2 experimental repeats. C) IVIS of fLuc-expressing P14 CD8 T cells in representative mice from the indicated conditions. n = 3 (Ag OFF, Ag OFF/CPI); 4 (Ag ON); or 5 (Ag ON/CPI), representative of > 3 experimental repeats. D) Average ± s.d. of radiance in the ROIs shown in C. * $P = 0.0228$ by two-tailed *t* test. n = 4 (Ag ON) or 5 (Ag ON/CPI), representative of > 3 experimental repeats. E) Confocal microscopy of skin from the indicated conditions. Dotted line = epidermis (top)/dermis (bottom) interface. n = 3, representative of 2 experimental repeats. F) Average ± s.d. of Ag (GFP)-expressing skin cell frequencies from the indicated conditions. * $P = 0.0360$, ** $P = 0.0043$ (Ag ON vs. Ag ON/CPI), ** $P = 0.0019$ (Ag ON/CPI + αCD8 vs. Ag OFF), **** $P < 0.0001$, and ns = not significant by two-tailed *t* test. n = 5 (Ag OFF, Ag OFF/CPI); 6 (Ag ON/CPI + αCD8); or 7 (Ag ON, Ag ON/CPI), representative of > 3 experimental repeats. G) Average ± s.d. of Ag (GFP)-expressing skin cell counts from the indicated conditions. **** $P < 0.0001$ and ns = not significant by two-tailed *t* test analysis of EpCAM+CD45- cells. n = 3, representative of > 3 experimental repeats.

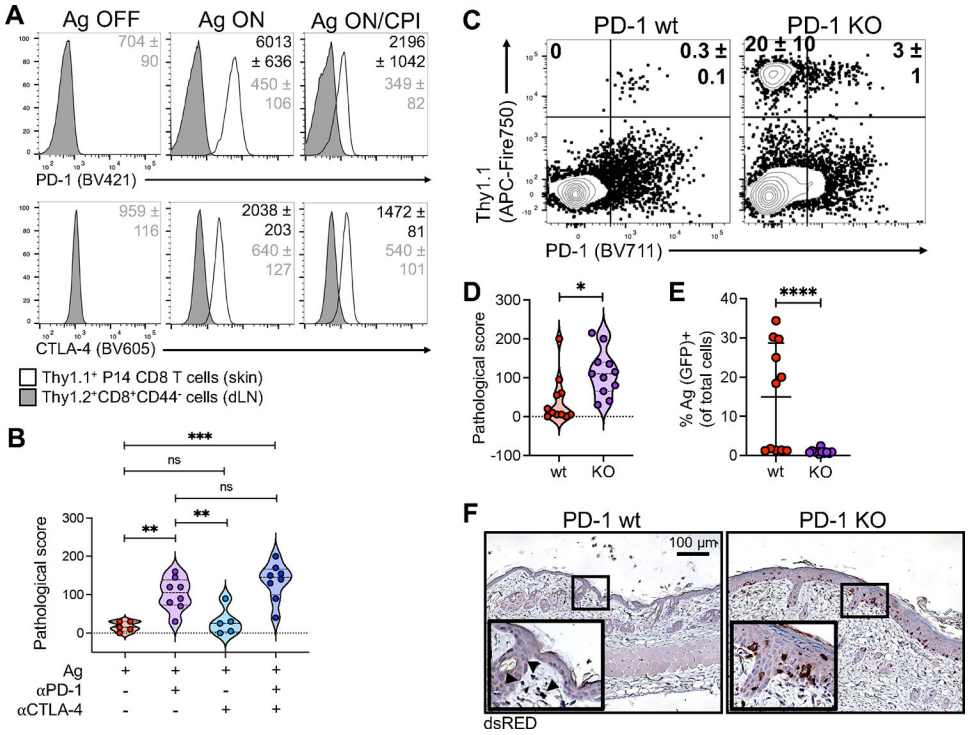

Figure 3 - PD-1 prevents epidermal infiltration and cutaneous disease by skin Ag-specific CD8 T cells

A) Average ± s.d. of MFIs of PD-1 and CTLA-4. n = 5, Representative of > 3 experimental repeats. B) Pathological scores by experimental condition. ** $P = 0.0013$ (Ag ON/αPD-1 vs. Ag ON), ** $P = 0.0096$ (Ag ON/αPD-1 vs. Ag ON/αCTLA-4), *** $P = 0.0003$ (Ag ON/CPI vs. Ag ON), and ns = not significant by two-tailed *t* test. n = 5 (Ag ON, Ag ON/αCTLA-4) or 8 (Ag ON/αPD-1, Ag ON/CPI), representative of 2 experimental repeats. C) Average ± s.d. of frequencies of skin-infiltrating Thy1.1+dsRED+ PD-1 wt or PD-1 KO P14 CD8 T cells. n = 5, representative of 2 experimental repeats. D) Pathological scores by experimental condition. * $P = 0.0124$ by two-tailed *t* test. n = 11, pool of 2 experimental repeats. E) Frequency ± s.d. of Ag (GFP)-expressing total skin cells from mice in D. **** $P < 0.0001$ by two-tailed Mann Whitney test. n = 11, pool of 2 experimental repeats. F) dsRED IHC staining of skin sections from mice in D. Representative of 2 experimental repeats.

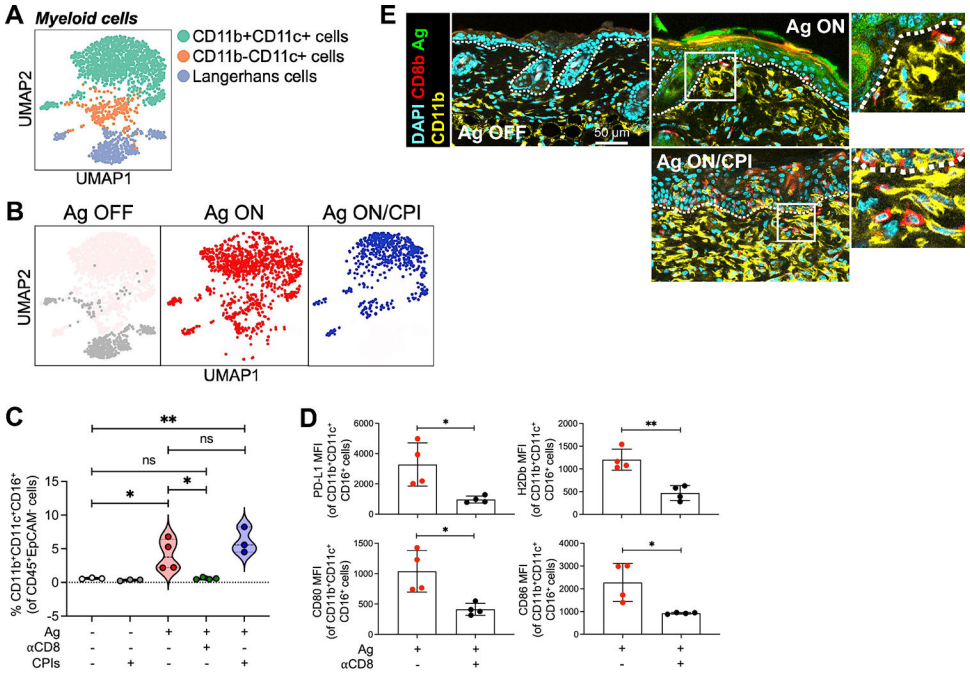

Figure 4 - Ag induction in skin leads to local CD8 T cell-myeloid cell modulatory interactions

A) UMAP projection of myeloid cell populations across experimental samples. B) UMAP projections of myeloid cell populations in A by experimental condition. C) Average ± s.d. of frequencies of skin-infiltrating CD11b+CD11c+CD16+ cells in the indicated conditions. * P = 0,0487 (Ag ON vs. Ag OFF), * P = 0.0216 (Ag ON + αCD8 vs. Ag ON), ** P = 0.0076 (Ag ON/CPI vs. Ag OFF), and ns = not significant by two-tailed t test. n = 3 (Ag OFF, Ag OFF/CPI, Ag ON/CPI) or 4 (Ag ON, Ag ON + αCD8), representative of 3 experimental repeats. D) Average ± s.d. of MFIs of the indicated surface markers expressed by skin-infiltrating CD11b+CD11c+CD16+ cells from the indicated conditions. * P = 0.0187 (PD-L1), * P = 0.0181 (CD86), * P = 0.0124 (CD80), and ** P = 0.0020 (H2Db) by two-tailed t test. n = 4, representative of 2 experimental repeats. E) Confocal microscopy of skin sections from the indicated conditions. Dotted line = epidermis (top)/dermis (bottom) interface. n = 3, representative of 2 experimental repeats.

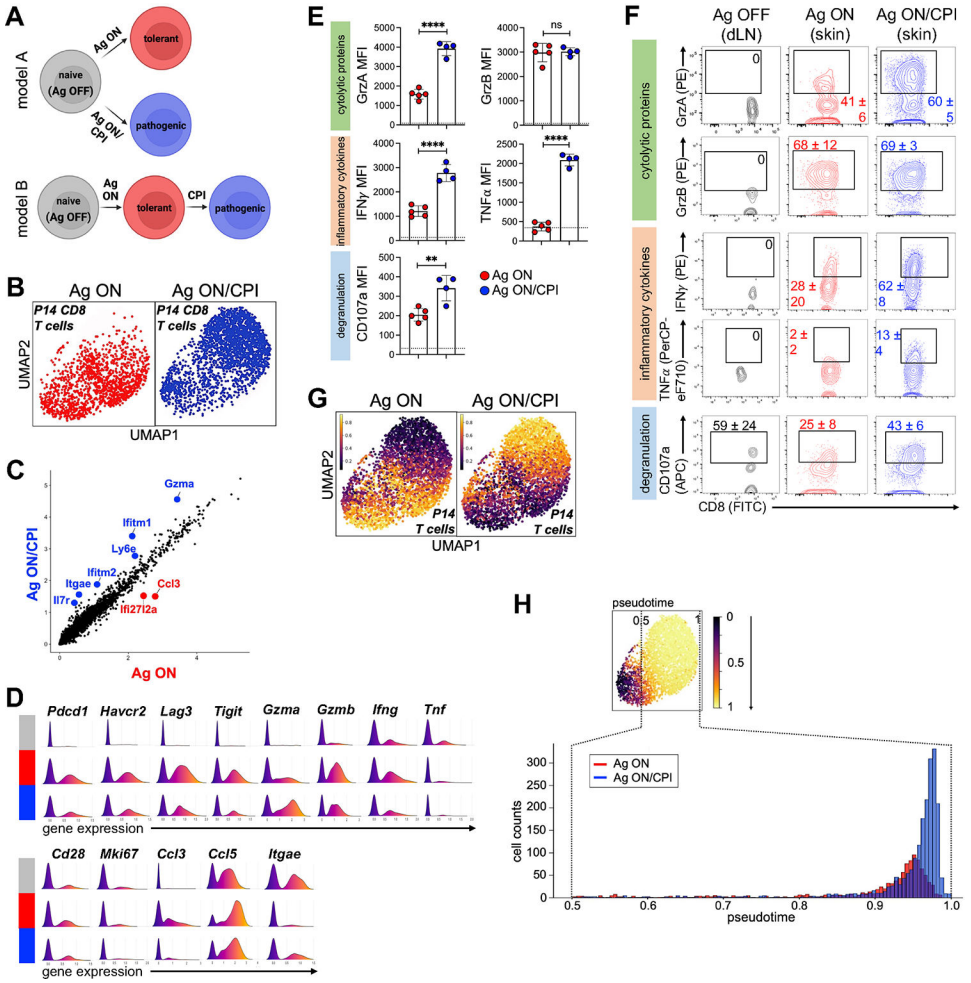

Figure 5 - Tolerant and pathogenic skin Ag-specific CD8 T cells are different states along the same differentiation trajectory

A) 2-model hypothesis of skin Ag-specific CD8 T cell differentiation. B) UMAP projections of skin-infiltrating P14 CD8 T cells by experimental condition. C) Scatter plot of total gene expression levels in skin-infiltrating P14 CD8 T cells from B. D) Expression levels of the indicated genes in skin-infiltrating P14 CD8 T cells from B (red = Ag ON; blue = Ag ON/CPI). Expression levels in total skin-infiltrating CD8 T cells are shown for Ag OFF (grey). E) Average ± s.d. of MFIs shown for skin-infiltrating P14 CD8 T cells from the indicated conditions after *ex vivo* restimulation with GP33 peptide. Dotted line = average MFI of P14 CD8 T cells from the dLNs of Ag OFF mice. ** $P = 0.0044$, **** $P < 0.0001$, and ns = not significant by two-tailed *t* test. n = 4 (Ag ON/CPI) or 5 (Ag OFF, Ag ON), representative of > 3 experimental repeats. F) Average ± s.d. of frequencies of gated skin-infiltrating P14 CD8 T cells from the indicated conditions after *ex vivo* restimulation with GP33 peptide. n = 5, representative of > 3 experimental repeats. G) MELD analysis quantifying likelihood of skin-infiltrating P14 CD8 T cells from B by experimental condition. H) Pseudotime analysis and cell number distribution along the pseudotime for skin-infiltrating P14 CD8 T cells in B.

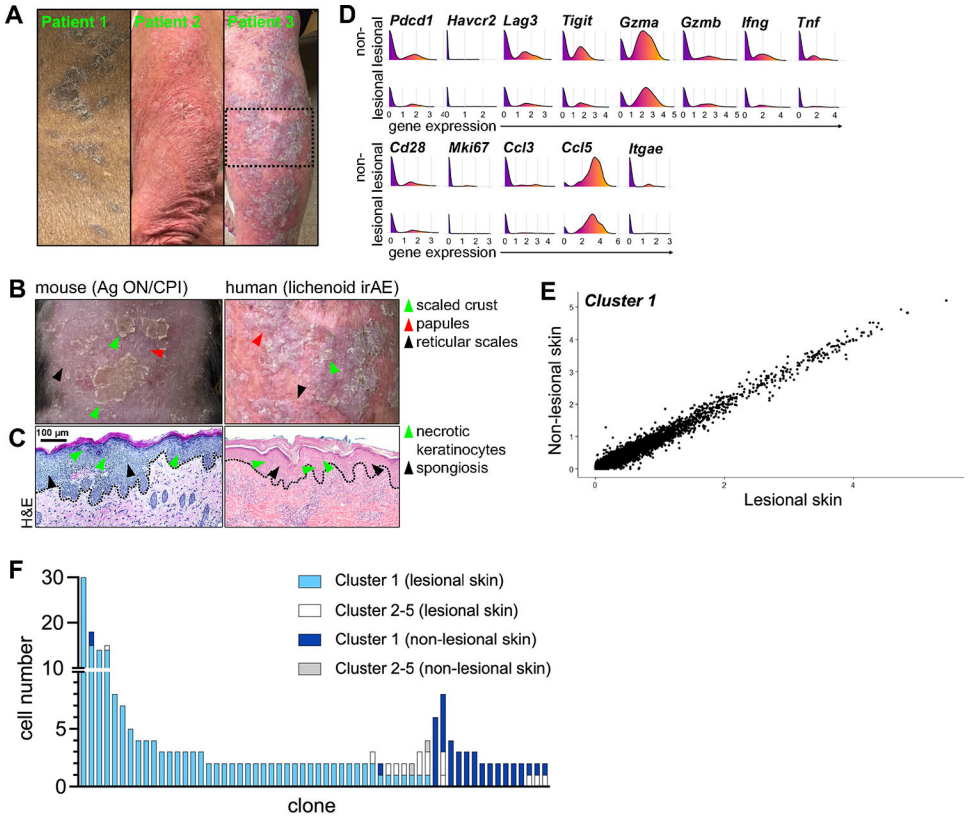

Figure 6 - Cytotoxic CD8 T cells are found in healthy human skin and are likely drivers of cutaneous lichenoid irAEs

A) Representative pictures of cutaneous lesions in patients diagnosed with lichenoid irAEs. Dotted square highlights the skin region shown in B. B,C) Representative macroscopic features (B) and histological features (C) of cutaneous pathology in an Ag ON/CPI mouse vs. human lichenoid irAE (from patient in A). Dotted line = epidermis (top)/dermis (bottom) interface. n = 6 (Ag ON/CPI mice) or 3 (human patients). D) Expression levels of the indicated genes in cytotoxic CD8 T cells (Cluster 1 from Extended Data Figure 10) sequenced in lesional and non-lesional skin from lichenoid irAE patients. E) Scatter plot of total gene expression levels in cytotoxic CD8 T cells from Cluster 1 sequenced in lesional vs. non-lesional skin from lichenoid irAE patients. F) Number and size of T cell clones containing cells from Clusters 1–5 (from Extended Data Fig 10) in lesional and non-lesional skin from lichenoid irAE patients.